JEM Journal of Experimental Medicine

BRIEF DEFINITIVE REPORT

Targeting CD206+ macrophages disrupts the establishment of a key antitumor immune axis

Arja Ray[1,2], Kenneth H. Hu[1,2], Kelly Kersten[1,2], Tristan Courau[1,2], Nicholas F. Kuhn[1,2], Itzia Zaleta-Linares[1,2], Bushra Samad[2,3], Alexis J. Combes[1,2,3,4], and Matthew F. Krummel[1,2,3]

CD206 is a common marker of a putative immunosuppressive "M2" state in tumor-associated macrophages (TAMs). We made a novel conditional CD206 (*Mrc1*) knock-in mouse to specifically visualize and/or deplete CD206+ TAMs. Early depletion of CD206+ macrophages and monocytes (Mono/Macs) led to the indirect loss of conventional type I dendritic cells (cDC1), CD8 T cells, and NK cells in tumors. CD206+ TAMs robustly expressed CXCL9, contrasting with stress-responsive *Spp1*-expressing TAMs and immature monocytes, which became prominent with early depletion. CD206+ TAMs differentially attracted activated CD8 T cells, and the NK and CD8 T cells in CD206-depleted tumors were deficient in *Cxcr3* and cDC1-supportive *Xcl1* and *Flt3l* expressions. Disrupting this key antitumor axis decreased tumor control by antigen-specific T cells in mice. In human cancers, a CD206^{Replete}, but not a CD206^{Depleted} Mono/Mac gene signature correlated robustly with CD8 T cell, cDC1, and NK signatures and was associated with better survival. These findings negate the unqualified classification of CD206+ "M2-like" macrophages as immunosuppressive.

Introduction

Macrophages have diverse roles in homeostasis and disease, and a refined understanding of the direct and indirect effects of targeting these cells in tumors is imperative, given the current impetus in developing myeloid targeting therapies for cancer (Binnewies et al., 2018; Goswami et al., 2023; Kowal et al., 2019; Pittet et al., 2022). While the pro-tumor effects of tumor-associated macrophages (TAMs) have been a dominant focus in the field, strategies for broad targeting of these cells and their monocyte precursors (Mono/Macs) and indeed those that are collectively known as myeloid-derived suppressor cells have met with limited success (Barry et al., 2023; Gomez-Roca et al., 2019). The detrimental effects of TAMs on antitumor immunity have indeed been highlighted by several critical studies (Broz et al., 2014; Doedens et al., 2010; Kersten et al., 2022; Mitchem et al., 2013; Nixon et al., 2022; Park et al., 2023; Peranzoni et al., 2018; Ruffell et al., 2014). However, TAMs can also act as organizing factors in antitumor immunity. One of the well-established ways macrophages aid antitumor immunity is by CXCL9/10/11 expression (House et al., 2020; Qu et al., 2020), which are ligands for CXCR3- expressing lymphocytes including CD8 T cells and natural killer (NK) cells. The importance of CXCL9 expressing TAMs in organizing immune cells in response to checkpoint blockade has been established in both mouse and human tumors (Bill et al., 2023; House et al., 2020; Qu et al., 2020). NK cells and activated CD8 T cells, on the other hand, are known to produce chemokines FLT3L and XCL1, supportive of conventional type 1 dendritic cells (cDC1s [Barry et al., 2018; Böttcher et al., 2018]). These cDC1s are well-characterized as antigen-presenting cells that potently stimulate CD8 T cells (Broz et al., 2014; Pittet et al., 2023; Salmon et al., 2016; Schenkel et al., 2021). Therefore, a cDC1:NK:CD8 T cell module is also associated with antitumor immunity and immune checkpoint blockade (ICB) (Barry et al., 2018; Böttcher et al., 2018). The context-dependent role of TAMs related to such modules of reactive immunity in the tumor microenvironment (TME) is not fully elucidated.

To design rational myeloid targeting strategies, there is a need to better understand the diversity and contextual function of macrophages. A widely used strategy for describing macrophage function in tumors has involved an "M1" versus "M2" nomenclature, derived from in vitro skewing with Th1 versus Th2 cytokines, and often equated with pro- and anti-

[1]Department of Pathology, University of California, San Francisco, CA, USA; [2]ImmunoX Initiative, University of California, San Francisco, CA, USA; [3]UCSF CoLabs, University of California, San Francisco, CA, USA; [4]Department of Medicine, University of California, San Francisco, CA, USA.

Correspondence to Matthew F. Krummel: matthew.krummel@ucsf.edu

K.H. Hu's current affiliation is Department of Immunology, The University of Texas MD Anderson Cancer Center and James P Allison Institute, Houston, TX, USA. K. Kersten's current affiliation is Cancer Metabolism and Microenvironment Program, Sanford Burnham Prebys Medical Discovery Institute, La Jolla, CA, USA.

inflammatory functions, respectively. Important studies including those that have established the dynamics of myeloid differentiation in tumors and the diversity of intratumoral Mono/Macs in murine and human tumors (Cheng et al., 2021; Ginhoux et al., 2016; Yofe et al., 2023) indicate that this binary M1/M2 delineation of macrophage phenotype does not capture the heterogeneity at the single cell level (Azizi et al., 2018; Cheng et al., 2021; Mujal et al., 2022). In wound healing, *Arg1* and *Mrc1* (gene corresponding to the mannose-binding C-type lectin CD206), both utilized as markers of an M2 state, have distinct expression patterns (Hu et al., 2023). There is also a lack of correlation among genes within the M1 or M2 signatures in Mono/Macs (Mujal et al., 2022), and M1 and M2 signatures in Mono/Macs often show correlated instead of opposing expression patterns in tumors (Azizi et al., 2018; Cheng et al., 2021).

Despite the evidence of transcriptomic data that suggests greater complexity than this nomenclature acknowledges, there is a lack of direct functional evidence to elucidate the roles of macrophages bearing one or more of these "M2" markers in tumors. As a result, Mono/Macs expressing "M2" markers such as CD206, sometimes designated as "M2-like," continue to be used as a marker of an immunosuppressive state. A holistic dissection of the role of CD206-expressing Mono/Macs and the precise effects of targeting them in tumors in vivo is, however, yet to be undertaken. We therefore developed a conditional knock-in reporter mouse using the *Mrc1* (CD206) allele that allows specific visualization and depletion of those cells to test how CD206$^+$ Mono/Macs contribute to antitumor immunity.

Results and discussion

A novel genetic tool to mark and deplete CD206-expressing macrophages

To highlight CD206 surface expression variation across Mono/Mac differentiation in tumors, we identified relevant subsets from previously published single-cell transcriptomics in B16F10 tumors (Fig. 1 A; Mujal et al., 2022) and applied flow cytometry to gate on those populations in a related B78chOVA (Kersten et al., 2022; where B78 is an amelanotic clone of B16 to allow imaging of tumors, chOVA is an mCherry and OVA construct) tumor model. CD206 was most prominently expressed by terminal VCAM-1^{hi}IL-7Rα^{lo} C1q TAMs (Fig. 1, B and C) (Mujal et al., 2022) followed by the VCAM-1^{lo}IL-7Rα^{hi} stress-responsive population (Fig. 1, B and C; associated with enriched glycolysis, increased *Arg1* and *Il7r* expression [Bill et al., 2023; Mujal et al., 2022], and possibly hypoxic [Wei et al., 2021]), where TAMs were defined as CD45$^+$Lin(CD90.2, Ly6G, B220, NK1.1, Siglec-F)$^-$Ly6C$^-$F480$^+$CD24$^-$ (Fig. S1 A). In contrast, CD206 was expressed at low levels by other less differentiated VCAM^{lo}IL-7Ra^{lo} double negative (DN) TAMs (Fig. 1, B and C). Among monocytes, defined as CD45$^+$Lin(CD90.2, Ly6G, B220, NK1.1, Siglec-F)$^-$Ly6C$^+$ (Fig. S1 A), the MHCII$^+$ subset was the prominent CD206 expressor as opposed to early (immature, MHCII$^-$) monocytes, albeit at lower levels than stress and C1q TAMs (Fig. 1, B and C). Overall, this analysis showed that CD206 is variably expressed across multiple monocyte and macrophage subsets and generally increases with Mono/Mac differentiation. Further, when considering the use of this protein and the gene encoding it as a means of eliminating these Mono/Macs and thereby studying their function, we noted that this scavenger receptor is frequently also expressed on other cells including endothelial cells and keratinocytes (Chi et al., 2003; Szolnoky et al., 2001) and may further be ectopically produced by other cells in the TME.

We thus generated a conditional system where a lineage-specific Cre could drive the recombination of a 3′ knock-in *Mrc1*$^{LSL\text{-}Venus\text{-}DTR}$ allele (Venus: yellow fluorescent protein variant for visualization; DTR: diphtheria toxin receptor for depletion) in mice (Fig. 1 D). Then, using a *Csf1r*^{Cre}; *Mrc1*$^{LSL\text{-}Venus\text{-}DTR}$ cross (DTR), compared with a *Mrc1*$^{LSL\text{-}Venus\text{-}DTR}$ (WT) control (Fig. 1 D), we assessed the reporter expression in various immune and CD45$^-$ non-immune compartments in the subcutaneous melanoma model B78chOVA (Fig. 1 E). Around 70% of TAMs showed robust Venus reporter expression tightly correlated with the surface expression of CD206 protein (Fig. 1 E). Following the CD206 expression patterns in the subsets of TAMs (Fig. 1 C), reporter expression was also highest in the VCAM-1^{hi}IL-7Rα^{lo} C1q TAMs, followed by the stress-responsive, and lowest in the VCAM^{lo}IL-7Ra^{lo} "DN" TAMs (Fig. 1 G). Likewise, a subset of CD206$^+$ monocytes expressed the reporter, consistent with *Csf1r*-driven expression (Fig. 1 E). Reporter expression within the monocytes was also predictably higher in the MHCII$^+$ mature subset (Fig. 1 G), with early monocytes being CD206$^-$ (Fig. 1 C). Apart from the CD206$^+$ Mono/Macs we intended to target, we also found that nearly half of the cDC2s (gated as CD45$^+$Lin(CD90.2, Ly6G, B220, NK1.1, Siglec-F)$^-$Ly6C$^-$F480$^-$CD24$^+$CD11c$^+$MHCII$^+$CD11b^{hi}CD103^{lo}) (Fig. S1 A) expressed the reporter along with CD206 in this system (Fig. 1 E), consistent with these being of monocytic origin and perhaps also being a population of cells sometimes called DC3s (Dutertre et al., 2019; Liu et al., 2023). Weaker expression was also found in the CD206$^+$ population of neutrophils (Fig. 1 E). Likewise, in the proximal tumor-draining lymph nodes (tdLN), the same hierarchy of expression patterns was observed, albeit with lower levels of CD206 and Venus expression (Fig. S1 B).

As a result of the *Csf1r*^{Cre} cross, reporter expression in tumors was observed only in these myeloid cells and not in CD206$^+$ non-immune cells, lymphocytes, and cDC1s (Fig. 1, E and F). Within the myeloid populations, expression of the Venus marker in CD206$^+$ TAMs was ∼2–3× brighter than the CD206$^+$ subsets of other myeloid cells, while that in the CD206$^-$ populations, it was negligible (Fig. 1 F). Further, the contribution of Venus reporter-positive cells in the tumor was heavily dominated by Mono/Macs, which made up about 95% of the intratumoral Venus$^+$ cells in a typical B78chOVA tumor (Fig. 1 H). In fact, specifically, the CD206$^+$ Mono/Macs made up >90% of the reporter-expressing cells in this tumor model, with CD206$^+$ macrophages alone making up >70% (Fig. 1 I). Combined with the increased reporter expression in the CD206$^+$ TAMs, as compared with the other myeloid subsets (Fig. 1 F), this demonstrates a highly penetrant system to mark and effectively deplete CD206$^+$ Mono/Macs in the TME, while sparing the CD206$^-$ counterparts. In contrast, when we tracked reporter expression in the same tumor model in a *LysM*^{Cre} cross, we found similarly no expression in the CD45$^-$ cells, lymphocytes, and cDC1s, but lower

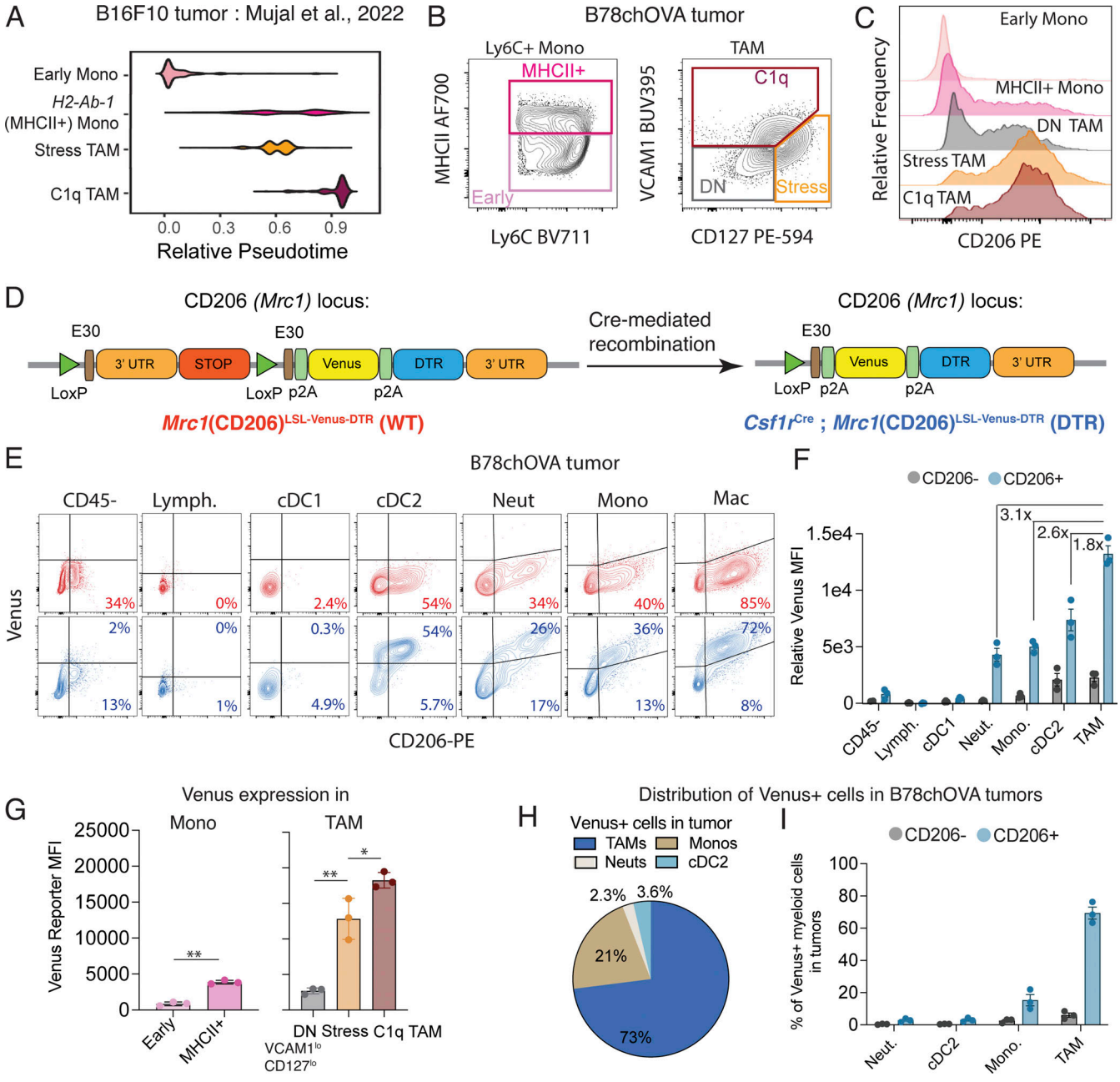

Figure 1. **Genetic myeloid-specific labeling of CD206⁺ macrophages in tumors. (A)** Pseudotime plots of select Mono/Mac subsets in B16F10 tumors from Mujal et al. (2022). **(B and C)** (B) Gating on the equivalent subsets in B78chOVA tumors by flow cytometry and (C) CD206 expression in each of these subsets. **(D)** Schematic representation of the *Mrc1*$^{LSL\text{-}Venus\text{-}DTR}$ knock-in construct before (WT) and after (DTR) Cre-mediated recombination by crossing to the *Csf1r*^{Cre} allele. **(E and F)** (E) Flow cytometry plots showing reporter (Venus) and CD206 expression in different immune cells in d18 B78chOVA tumors in WT (red) and DTR (blue) mice with (F) quantification of relative reporter expression (DTR – WT) in the different immune cells, segregated by CD206 expression. Fold change of relative reporter expression between the CD206⁺ populations of the different myeloid subsets are noted. **(G)** Reporter expression of the monocyte and TAM subsets shown in B. **(H and I)** (H) Average distribution of Venus reporter expressing cells in a typical B78chOVA tumor at d18 and (I) corresponding distribution segregated by CD206 expression. Bar graphs show mean ± SEM (F, G, and I); data are representative of at least two independent experiments, each with at least three biological replicates; WT levels averaged from two biological replicates in F; *P < 0.05, **P < 0.01 by paired *t* test and RM ANOVA and post-hoc *t* tests in G.

expression in the neutrophils, and only marginal expression in the cDC2s (Fig. S1 C). However, we also noted suboptimal penetrance in our target population with this strain, with only about 35–40% of the CD206⁺ Mono/Macs expressing the reporter (Fig. S1 C).

Given our goal to target CD206⁺ macrophages, we therefore, adopted the *Csf1r*^{Cre} cross to investigate the effects of targeting CD206⁺ Mono/Macs in the TME. We estimated a high (>90%) penetrance in these specific intratumoral CD206⁺ Mono/Mac populations in B78chOVA tumors from the data above. We

further estimated a potential effect on CD206⁺ cDC2s and neutrophils, although the strength of reporter expression was 2–3× lower in these CD206⁺ myeloid cells (Fig. 1 F). Importantly, this system would have no direct impact on lymphocytes, CD206⁺ non-immune cells, and CD206⁻ myeloid cells, including cDC1s.

Early CD206⁺ TAM depletion leads to the indirect loss of antitumor immune cells

To test the impact of CD206⁺ macrophage targeting on the overall tumor immune microenvironment, we took advantage of the linkage of Venus and DTR expression in this background to deplete those cells. In our setup, using subcutaneous B78chOVA tumors as described previously, adoptively transferred OVA-specific OT-I cells allow the tracking of antigen-specific CD8 T cell responses, which nevertheless do not mediate tumor control (Kersten et al., 2022; Ray et al., 2023, *Preprint*). We first confirmed that Cre-mediated induction of reporter expression without diphtheria toxin (DTx) administration did not alter the immune composition of these OVA-expressing tumors with OT-I transfer in the WT (*Mrc1*$^{LSL\text{-}Venus\text{-}DTR}$) versus DTR mice (*Csf1r*^{Cre}; *Mrc1*$^{LSL\text{-}Venus\text{-}DTR}$) (Fig. S2 A). With this baseline, we administered DTx either "late/acute," namely in the last 4 days prior to the tumor harvest or "early/chronic," i.e., every day for 2–3 days, starting 2 days after T cell injection until harvest to parse out the role of CD206⁺ Mono/Macs in the TME (Fig. 2 A). These two modes of depletion represent perturbations at different phases of maintenance and establishment of the tumor immune microenvironment, respectively.

In the context of late DTx administration, we found that this regimen specifically depleted the cells of interest and otherwise had little overall effect on other non-targeted cells. Thus, there was a large reduction in the TAMs (Fig. 2 B), which corresponded to a specific and penetrant loss (~95%) of the CD206⁺ but not the CD206⁻ population (Fig. 2 I). We found a compensatory rise in monocytes overall (Fig. 2 C), as may be expected through mobilization of circulating and bone marrow–derived cells (Kodumudi et al., 2010) following the depletion of CD206⁺ TAMs. No significant loss was observed in cDC2s and neutrophils overall (Fig. 2, D and E). In all these myeloid subsets, the relative loss of CD206⁺ subsets was variable (Fig. 2 R)—most robust in the TAMs, followed by monocytes, cDC2s, and weakest in neutrophils. This is consistent with the relative strength of reporter expression in the CD206⁺ subsets of these myeloid cells, as shown in Fig. 1 F. Thus, direct depletion was heavily biased to the highest expression of the construct, namely the CD206⁺ TAMs. Barring the compensatory increase in monocytes, this depletion of CD206⁺ TAMs in an established tumor immune microenvironment had no discernible indirect impact at the population level, particularly on the abundance of three key antitumor immune cells—cDC1 (Fig. 2 F), NK cells (Fig. 2 G), and tumor antigen-specific CD8 T cells (Fig. 2 H).

When we depleted CD206⁺ populations with DTx early, i.e., starting 2 days after OTI adoption, we found robust depletion of TAMs (Fig. 2 J), again with a specific and penetrant (~85%) loss of those expressing CD206, leaving CD206⁻ TAMs unchanged (Fig. 2 Q). No overall increase in monocytes was observed here (Fig. 2 K) and the compensatory increase associated with CD206⁺ macrophage loss was instead in the neutrophil compartment (Fig. 2 M), while overall cDC2 abundance was once again unchanged (Fig. 2 L). CD206⁺ subsets of these other myeloid populations were again variably depleted—significantly in monocytes and cDC2s and mildly in neutrophils (Fig. 2 S). In contrast to the late depletion setting, here, we observed a significant decrease in intratumoral abundance of cDC1 (Fig. 2 N), NK cells, and transferred OT-Is in the tumor (Fig. 2, O and P). Therefore, early DTx administration led to the direct depletion of CD206⁺ Mono/Macs and CD206⁺ cDC2, indirect increase in neutrophils, along with the indirect loss of cDC1s, NK cells, and CD8 T cells.

These trends in abundances were similar when expressed as a percentage of live cells (Fig. S2, B and C), indicating numerical changes, in all cases, except the increase in monocytes following acute depletion, which only trended higher. When we similarly treated non-tumor bearing DTR mice with six doses of DTx akin to the early depletion regimen in tumors and analyzed the immune compositions in the skin (site of the ectopic tumor injections) (Fig. S2 D), no robust indirect loss of populations was observed, but an increase of neutrophils in an otherwise scarcely immune-populated skin was recorded (Fig. S2 E). This demonstrates that the important indirect effects on lymphocytes and cDC1s were not a result of repeated DTx exposure alone.

Given the associated increase in neutrophils in long-term DTx treated conditions, we repeated the same early depletion experiment in tumors, now with the addition of anti-Ly6G neutrophil depleting antibody or isotype control (Fig. S2 F) to assess whether the gained neutrophils played a role in the indirect loss of lymphocytes and cDC1s. As expected, both in terms of the total number of cells per gram of tumor (Fig. S2 G) and the percentage of CD45⁺ (immune) cells (Fig. S2 H), the abundance of immune cell types in WT and DTR mice treated with isotype control mirrored those of the early depletion regimen. With anti-Ly6G treatment in DTR mice, neutrophils were reduced to levels below those of isotype-treated controls (Fig. 2 T and Fig. S2 G), without any concomitant effect on the indirect depletion of cDC1s, NK cells, and OT-I T cells (Fig. 2 U and Fig. S2 G).

In recent important work on monocyte-derived cDC2s or DC3s, these cells have been shown to express CD206 (Liu et al., 2023) and to support CD8 T cells with a tissue-resident memory T cell (T_{RM})-like phenotype (Bourdely et al., 2020) in contexts where such T cells are well-defined. We therefore investigated whether this axis may be at play in our early depletion setting. First, we found no difference in the T_{RM}-like CD44⁺CD69⁺CD103⁺ abundance among CD8 T cells in the early depletion condition (Fig. S2 I), showing that T cells of this phenotype are not specifically lost due to the depletion. Further, we investigated early depletion in the *LysM*^{Cre} crossed model, where CD206⁺ cDC2s do not express high levels of the reporter (Fig. 1 C). Here, we found significant yet incomplete direct depletion of CD206⁺ TAMs (~45%) (Fig. S2 J) but no depletion of CD206⁺ cDC2s (Fig. 2 V and Fig. S2 K) along with unchanged monocyte and increased neutrophil abundance (Fig. S2, L and M). Importantly, with this incomplete depletion of CD206⁺ TAMs, we observed a significant decrease in cDC1 abundance (Fig. 2 W, along with more variability among tumors) and a trend

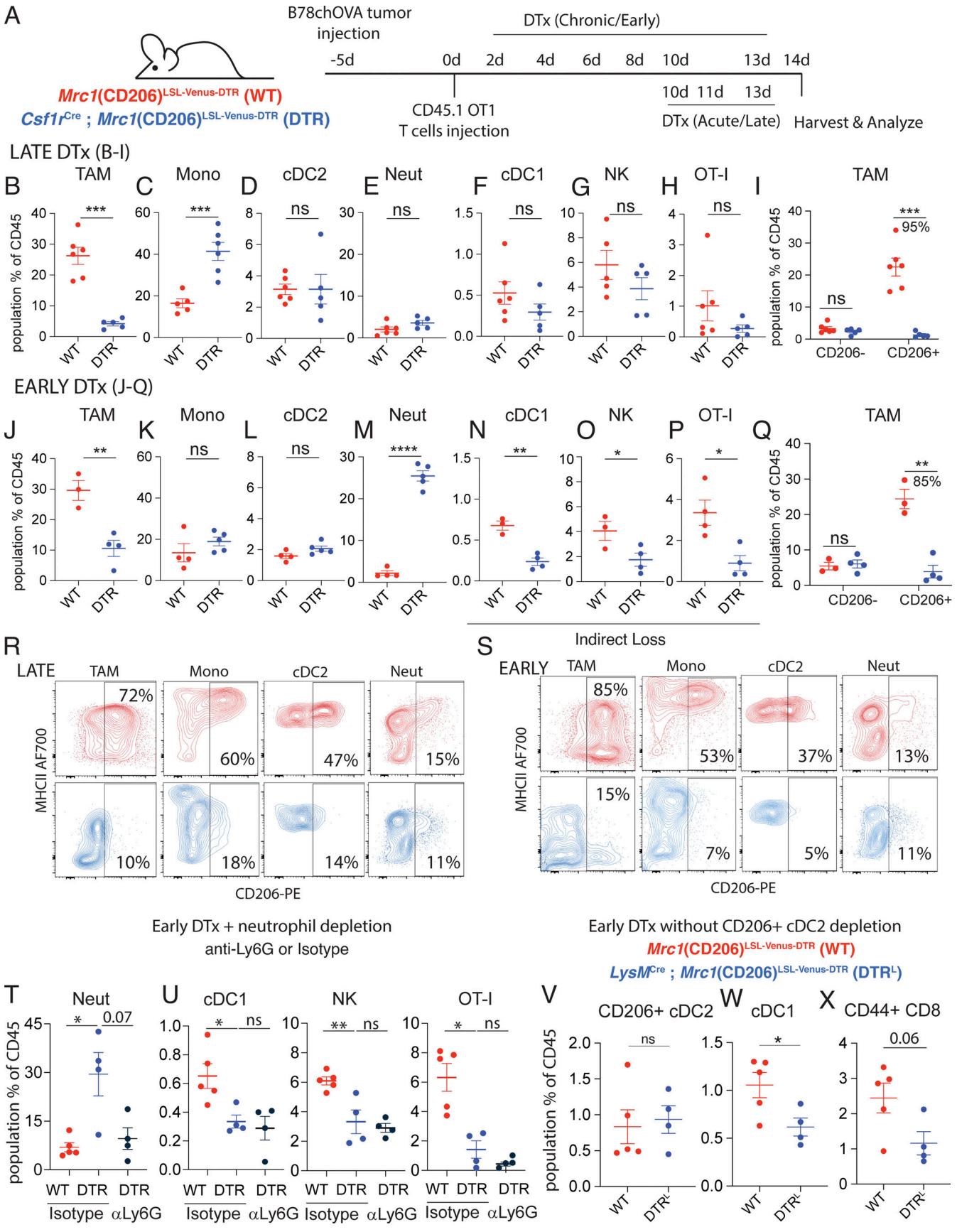

Figure 2. **Early CD206⁺ TAM depletion leads to a coordinated and indirect loss of NK, cDC1, and CD8 T cells in tumors. (A)** Schematic representation of the experimental setup for early and late CD206⁺ TAM depletion in B78chOVA tumors using *Mrc1*(CD206)$^{LSL\text{-}Venus\text{-}DTR}$ (WT) and *Csf1r*^{Cre}; CD206$^{LSL\text{-}Venus\text{-}DTR}$

(DTR) mice. **(B–H and J–P)** Relative abundance of different immune populations in B78chOVA tumors as a percentage of CD45⁺ cells with (B–H) late and (J–P) early depletion regimens. **(I and Q)** Abundance of TAMs gated by CD206 expression, showing percentage depletion of CD206⁺ TAMs in (I) late and (Q) early depletion setting. **(R–U)** Representative flow cytometry plots showing CD206 versus MHCII expression in different intratumoral myeloid subsets in WT (red) and DTR (blue) mice in the (R) late and (S) early depletion regimens; relative abundance of (T) neutrophils, (U) cDC1, NK cells, and OT-I T cells in the early DTx administration setting with additional anti-Ly6G or isotype control treatment. **(V–X)** Relative abundance of (V) CD206⁺ cDC2, (W) cDC1, and (X) CD44⁺ CD8 T cells in the early DTx administration setting in WT and DTR^{L} (*Lyz2*(LysM)^{Cre}; $CD206^{LSL\text{-}Venus\text{-}DTR}$) mice. Bar graphs show mean ± SEM; data are representative of at least two independent experiments, each with at least three biological replicates per group; ***P < 0.001, **P < 0.01, *P < 0.05, ns = no significance by unpaired Student's *t* tests or Mann–Whitney *U* test (B–Q and V–X) and Kruskal–Wallis test with post-hoc test correcting for false discovery rate (T and U).

toward decreasing antigen-experienced (CD44⁺) CD8 T cells in the tumor (Fig. 2 X), consistent with our other results using the $Csf1r^{Cre}$ cross.

These data suggest that the indirect lymphocyte and cDC1 loss was not due to CD206⁺ cDC2s or infiltrating neutrophils. As noted earlier, CD8 T cell, NK, and cDC1 populations form a virtuous module of antitumor immunity and are mechanistically linked to each other in the TME (Barry et al., 2018; Böttcher et al., 2018). Noting that none of this trifecta of immune cells express the reporter, we concluded that a direct, targeted ablation of "M2-like" CD206⁺ Mono/Macs by early DTx treatment led to the indirect loss of this key antitumor reactive module (Barry et al., 2018). Further, the decreased abundance of CD8 T cells and NK cells was not observed in the tdLN, indicating a tumor-specific mechanism (Fig. S2 N). These data suggested that CD206⁺ Mono/Macs were involved in the recruitment and early establishment of this module in the TME.

Early depletion skews Mono/Macs toward immature and hypoxic subsets

To define the macrophage subtypes associated with this reactive immune module and their potential spatially segregated modes of action, we performed spatial transcriptomics of B78chOVA tumors guided by Venus (CD206 reporter) expression. For this, we first spatially mapped the CD206⁺ macrophage population by Venus expression using two-photon microscopy of B78chOVA tumor slices with transferred OT-I T cells marked by the CD2dsRed allele (Fig. 3 A). Doing this revealed three distinct niches of CD206⁺ macrophage and T cell localization. The "edge," which is macrophage and collagen-rich with modest T cell presence (typically ∼300 µm from the tumor boundary), "mid," which is the interfacial layer with abundant T cell: macrophage interaction zones (∼300 µm zone contiguous to the "edge"), and "interior." The interior is sparser in both immune cell types but represents the bulk of the tumor by volume (Fig. 3 A). We then performed post-imaging spatial transcriptomics by ZipSeq (Hu et al., 2020) on CD45⁺ cells in these three zones (Kersten et al., 2022) of B78chOVA tumors, with or without early DTx treatment, harvested at day 12 after T cell injection. DTx-treated tumors lacked Venus-expressing cells, consistent with depletion (Fig. 3 A). UMAP projection of non-linear dimensional reduction and Louvain clustering clearly showed the shift in tumor immune composition among control and DTx-treated groups (Fig. 3, B and C; and Fig. S3 A). Notably, previously defined C1q and stress-responsive (Stress) TAMs, which most robustly express CD206 at the protein level, along with MHCII⁺ and ISG-expressing monocytes were expectedly depleted by direct DTx action (Fig. 3 C). The depletion of C1q TAMs (VCAM-1^{hi}IL-$7R\alpha^{lo}$) and MHCII⁺ monocytes were verified by flow cytometry using gating strategies described in Fig. 1 (Fig. 3 D). On the other hand, early monocytes, neutrophils, and an *Spp1*, *Hif1α*-expressing subset related to the Stress TAMs by shared expression of *Arg1*, *Il7r* (i.e., $Stress^{Spp1}$ TAM), became prominent in the DTx-treated condition (Fig. 3 C and Fig. S3 A). The loss of cDC1:NK:CD8 populations was again evident in the analysis of relative abundance from the single-cell RNA sequencing (scRNASeq) data (Fig. 3 C). Even though the small area of the tumor edge was much denser in the CD206⁺ Mono/Macs as shown by imaging, the transcriptomic data suggests high CD206-expressing C1q and Stress TAMs were more or equally as abundant in the interior than the edge (Fig. 3 E). This is consistent with the trajectory of increasing Mono/Mac differentiation toward the interior of the tumor (Kersten et al., 2022). The spatial distribution of myeloid cells in the tumor is likely model-dependent and may be quite different in spontaneous, autochthonous tumor models, as elegantly demonstrated in other contexts (Carmona-Fontaine et al., 2017; Laviron et al., 2022; Yofe et al., 2023). In this subcutaneous tumor model, the changes in immune subpopulations were not limited to a specific region of the tumor (Fig. 3 C) but permeated throughout as a consistent change in the tumor immune microenvironment. Thus, the transcriptomics data was congruent with the flow cytometry-based characterization of depletion effects and enabled further investigations into the key distinctions in the CD206-replete and depleted conditions.

CD206⁺ TAMs attract CXCR3-expressing, cDC1-supportive lymphocytes to the tumor

A well-established positive functional role of TAMs is the production of CXCL9 and CXCL10, inducing CXCR3-dependent lymphocyte recruitment in tumors (House et al., 2020). Given the indirect loss of lymphocytes upon early removal of CD206⁺ Mono/Macs, we hypothesized that this axis is prominent in these CD206-positive populations. Analyzing the single-cell sequencing (scSeq) data in detail, we found that expression of *Cxcl10* (Fig. S3 C) and *Cxcl9* (Fig. 3 G). in particular, were markedly reduced in the DTx-treated tumors, and this corresponded to substantial expression by the directly depleted subsets (CD206⁺MHCII⁺ Mono/Macs) and none of the indirectly increased ones (early mono, $Stress^{Spp1}$ TAM, and neutrophils) (Fig. S3 B and Fig. 3 F). We confirmed this finding by flow cytometry for intracellular CXCL9 expression in TAMs from WT and DTR mice with early depletion (∼50% decline, Fig. 3, H and I). This analysis further revealed a positive association between this chemokine and CD206 expression in B78chOVA TAMs (Fig. 3 J), resulting in a significant difference (again ∼50%) in CXCL9 expression in CD206⁺ versus CD206⁻ TAMs (Fig. 3 K) in

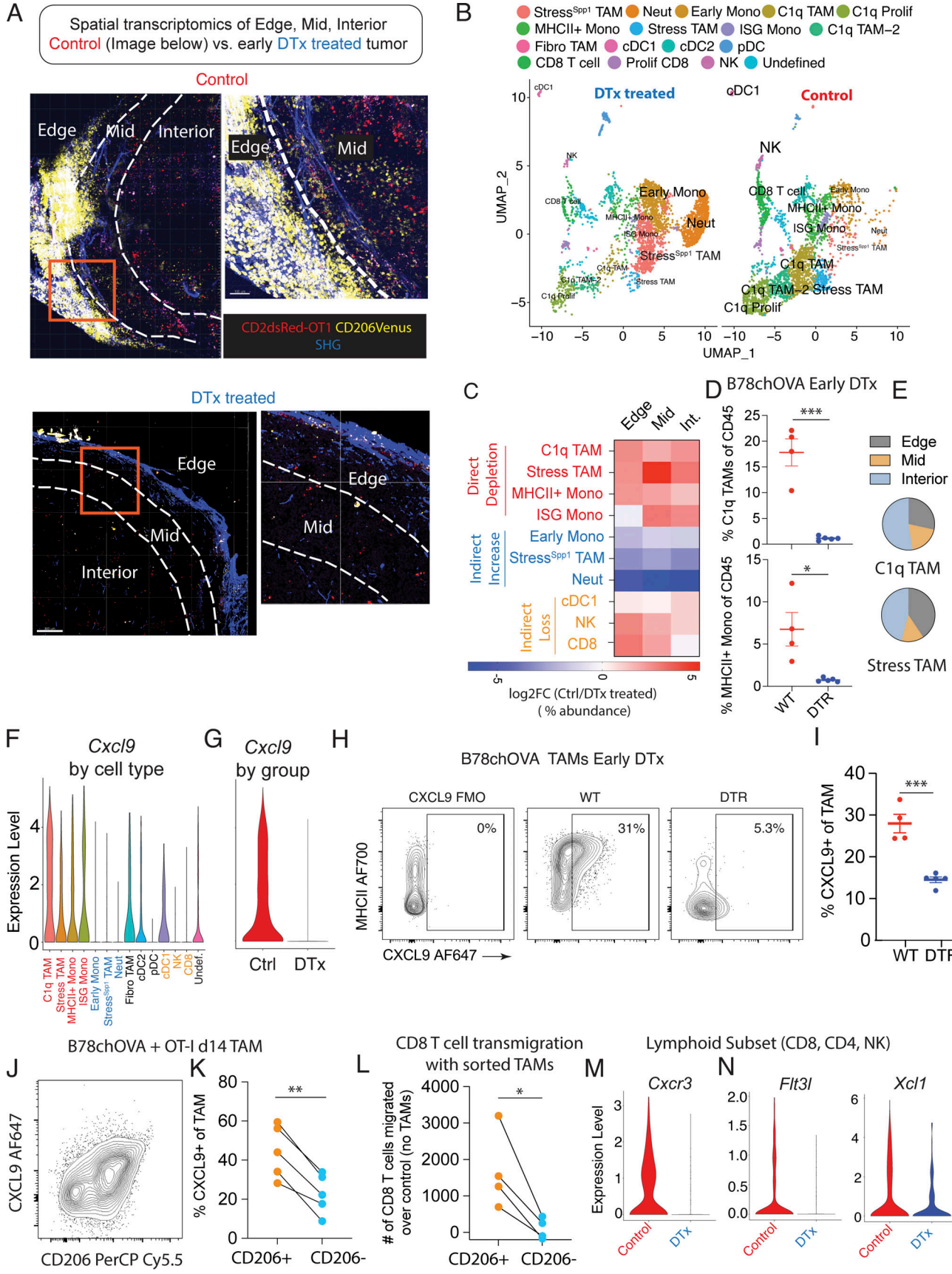

Figure 3. **Loss of CXCL9-positive TAMs and CXCR3-expressing, cDC1 supportive lymphocytes with CD206⁺ TAM depletion. (A)** Two-photon imaging of representative control and early DTx treated B78chOVA tumors day 12 after adoptive transfer of CD2dsRed; OT-I CD8 T cells showing three zones of Venus-

expressing macrophage and associated OT-I T cell localization—edge, mid, and interior (Int.) mapped by spatial transcriptomic barcoding ZipSeq. Boxed regions are magnified (right). Scale bars are 100 and 300 µm in the control (inset) and DTx-treated images respectively. **(B)** UMAP representation of major immune cell populations obtained from Control and early DTx treated B78chOVA tumors on day 12 after OT-I injection aggregated across all three regions. **(C)** Summary heatmap showing relative log fold change of the abundance (calculated as the percent of the total number of cells recovered within that region) of each major cluster in Ctrl/DTx treated conditions, split by region of tumor. **(D)** Flow cytometry data showing an abundance of C1q TAMs and MHCII$^+$ monocytes in Ctrl and DTx-treated conditions. **(E)** Distribution of C1q and Stress-responsive TAMs in the three spatial regions in control B78chOVA tumors. **(F and G)** *Cxcl9* expression (F) aggregated across treatment conditions by cluster and (G) aggregated across clusters by condition. **(H and I)** (H) Representative flow cytometry plots showing CXCL9 expression in TAMs in early DTx-treated WT and DTR B78chOVA tumors and (I) corresponding quantification. **(J and K)** (J) Representative flow cytometry plot showing intracellular CXCL9 versus surface CD206 expression in TAMs in B78chOVA tumors at day 14 after OT-I adoptive transfer without depletion, and (K) the same CXCL9 expression split by CD206 positivity. **(L)** In vitro–activated CD8 T cell migration at 3 h through a 5-µm transwell insert in the presence of sorted CD206$^+$ versus CD206$^-$ TAMs from B78chOVA tumors, normalized to migration with no TAMs. **(M and N)** (M) *Cxcr3*, (N) *Flt3l*, and *Xcl1* expression in the lymphocyte subset (CD8 T cell, NK cell, and CD4 T cell) by treatment group. Bar graphs show mean ± SEM; data are representative of at least two independent experiments, each with at least three biological replicates, except the spatial transcriptomics data (B, C, E–G, M, and N), from one control and one DTx-treated tumor; ***P < 0.001, **P < 0.01, *P < 0.05, ns = no significance by Mann–Whitney test (D), unpaired *t* test (I), and ratio paired *t* test (K and L).

the WT mice. This finding was substantiated in another subcutaneously injected tumor model MC38chOVA and the spontaneous breast tumor model PyMTchOVA (Engelhardt et al., 2012), both with lower overall CXCL9 positivity in the absence of OT-I adoptive transfer, but a consistent ∼50% or more difference between the CD206$^+$ and CD206$^-$ groups (Fig. S3 D). CD206$^+$ monocytes also expressed more CXCL9 compared with CD206$^-$ counterparts (Fig. S3 E), but CXCL9$^+$ monocytes were only one-fourth as abundant as CXCL9$^+$ TAMs in the B78chOVA TME, thus limiting their relative role in myeloid CXCL9 production (Fig. S3 F). Notably, CD206$^+$ cDC2s, which were also depleted in this condition, were not associated with CXCL9 expression (Fig. S3 G) and expressed lower levels than TAMs overall. We therefore sorted CD206$^+$ versus CD206$^-$ TAMs from B78chOVA tumors (day 14 after tumor injection without OT-I treatment) and interrogated their relative effects on in vitro activated (>90%) CXCR3-expressing (Fig. S3 H) CD8 T cell transmigration in a 3-h window. Consistent with their CXCL9 expression, the CD206$^+$ but not the CD206$^-$ TAMs induced enhanced transmigration of these activated CD8 T cells over no TAM-added controls. (Fig. 3 L). Since CD206 TAM-depleted tumors still had small numbers of lymphocytes, we compared their levels of CXCR3 at the transcript level, which reflects receptor-ligand engagement avoiding the confounding effect of receptor internalization (Meiser et al., 2008), and found that *Cxcr3* expression was markedly lower in the DTx-treated condition in all the lymphocyte subsets (Fig. 3 M and Fig. S3 I). Taken together, these data point to the role of CD206$^+$ TAMs in the recruitment of CXCR3-expressing lymphocytes to the TME, which is disrupted by DTx-mediated early depletion.

Lymphocytes are well-established as key producers of cDC1-formative chemokines FLT3L (Barry et al., 2018) and XCL1 (Böttcher et al., 2018). While NK cells are the most prominent producers of these chemokines and have been implicated in supporting and recruiting cDC1s to the tumor (Barry et al., 2018), activated CD8 T cells, such as those arriving in the tumor are also known to produce these chemokines. Therefore, given the loss of cDC1s in concert with lymphocytes with this depletion regimen, we probed for these chemokines in the intratumoral lymphocytes in the control versus CD206-depleted dataset. This demonstrated that both *Flt3l* and *Xcl1* (Fig. 3 N and Fig. S3 J) transcripts were markedly reduced in the NK cells and CD8 T cells in the DTx-treated condition. These changes on a per-cell basis, in addition to the overall decrease in CD8 T cells and NK cells, are consistent with the loss of cDC1s in the TME and resulting disruption of the CD8:NK:cDC1 module.

Depletion of CD206$^+$ TAMs thwarts CD8 T cell–mediated antitumor immunity in mice

Given our finding that targeting CD206$^+$ macrophages disrupts the organization of this important node of antitumor immunity, we asked whether their depletion would be detrimental to successful CD8 T cell–mediated tumor regression. To test this, we used an MC38chOVA (the same mCherry-OVA construct in an MC38 tumor cell line) model where an adoptive transfer of OT-I T cells results in efficient tumor control (Ray et al., 2023, *Preprint*) (Fig. 4 A). This contrasts with the B78chOVA model where adoptive transfer of OT-Is has no significant impact on tumor growth (Kersten et al., 2022), including both the early and late depletion regimens (Fig. S3 K). We then sought to investigate whether the same patterns of CXCL9-associated indirect loss of the key antitumor immune cells accompanied the targeting of CD206$^+$ TAMs in this model. We confirmed first that reporter expression in these tumors with the *Csf1r*^{Cre} cross followed largely the same pattern as the B78chOVA tumors, with substantial expression in CD206$^+$ TAMs and lower expression in the CD206$^+$ subsets of cDC2s, monocytes, and neutrophils (Fig. S3, L and M). Importantly, lymphocytes, cDC1s, and CD206$^-$populations of myeloid cells—again did not show significant reporter expression (Fig. S3, L and M). As with the B78chOVA model, CD206 expression increased with mature Mono/Mac differentiation states. CD206 expression was once again minimal in the early monocytes, modest in MHCII$^+$ activated monocytes and VCAM^{lo}CD127^{lo} "DN" TAMs, and higher in Stress TAM and C1q, as defined earlier (Fig. 4 B). The distribution of Venus reporter-positive cells (an estimate of the expected cells to be directly depleted) in these tumors was also heavily dominated by Mono/Macs, which made up about >95% of the intratumoral Venus$^+$ cells in a typical MC38chOVA tumor (Fig. 4 C). In particular, the CD206$^+$ Mono/Macs made up >95% of the reporter-expressing cells in this tumor model, with CD206$^+$ macrophages alone making up around 80% (Fig. 4 D).

With this confirmation of a similarly distributed CD206 expression in Mono/Macs and penetrant depletion strategy, we applied early and late depletion regimens to the MC38chOVA tumors. This was first done without the addition of OT-I T cells

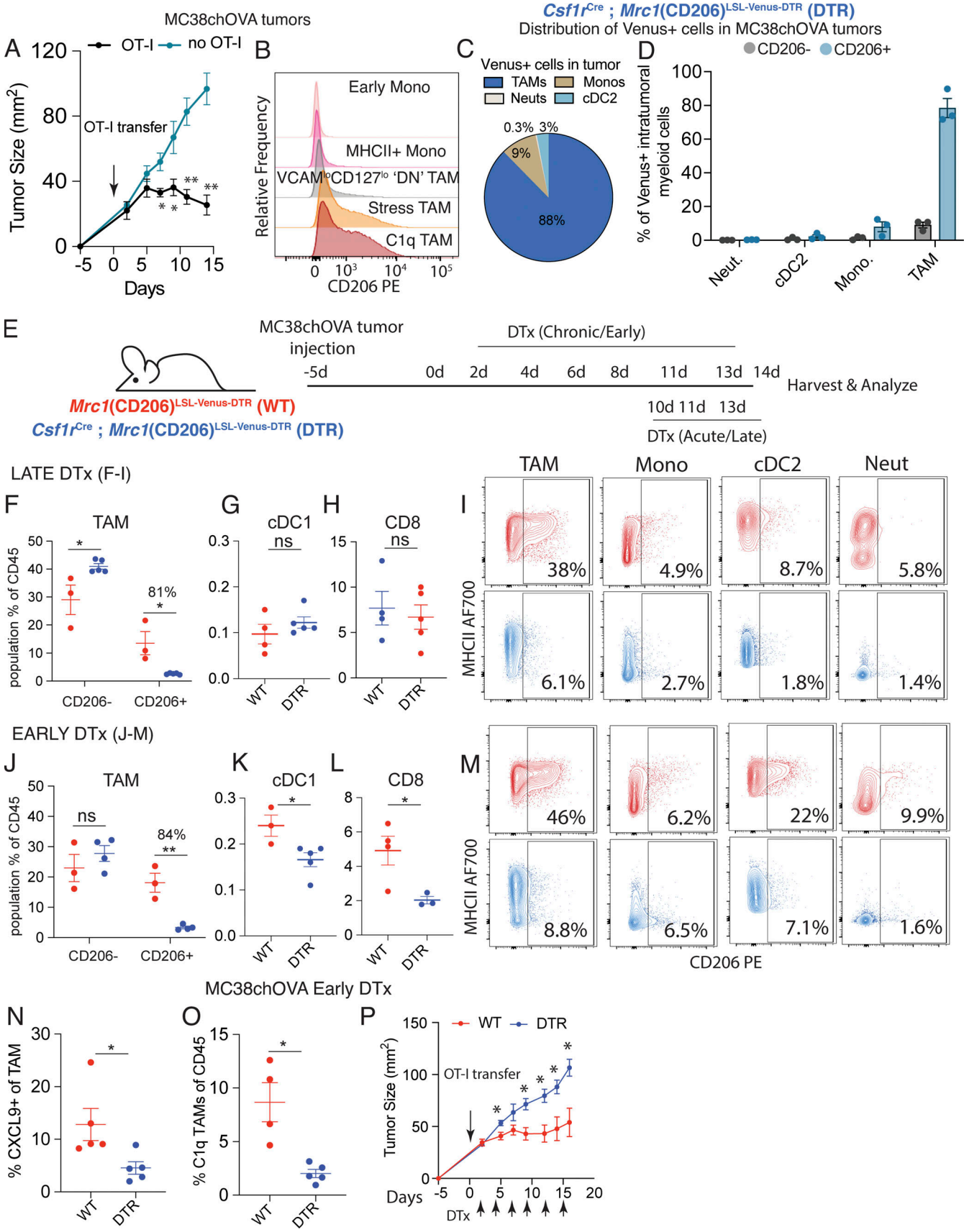

Figure 4. **CD206⁺ TAM depletion attenuates T cell–mediated tumor control in an immune-responsive tumor model. (A)** Representative time course of MC38chOVA tumor size with or without adoptive transfer of OT-I T cells. **(B)** CD206 expression in monocytes gated by MHCII expression and TAMs gated by

VCAM1 and CD127, as shown in Fig. 1 B, but in MC38chOVA tumors. **(C and D)** (C) Distribution of Venus reporter expressing cells in a typical MC38chOVA tumor at day 18 (d18) and (D) corresponding distribution segregated by CD206 expression. **(E)** Schematic representation of the experimental setup for early and late CD206$^+$ TAM depletion in MC38chOVA tumors using *Csf1r*^{Cre}; *Mrc1*$^{LSL\text{-}Venus\text{-}DTR}$ mice. **(F–H and J–L)** Relative abundance of (F and J) CD206$^+$ and CD206$^-$ TAMs, (G and K) cDC1s. and (H and L) CD8 T cells as a percentage of CD45$^+$ cells with late and early depletion regimens respectively. **(I and M)** Representative flow cytometry plots showing CD206 versus MHCII expression in different myeloid subsets in WT (red) and DTR (blue) mice in the (I) late and (M) early depletion regimens. **(N and O)** %CXCL9$^+$ of TAMs and (O) %C1q TAMs (gated as VCAM1^{hi}CD127^{lo}) of CD45 in WT and DTR mice with early depletion. **(P)** Tumor growth kinetics of MC38chOVA tumors in WT and DTR mice with DTx treatment beginning 2 days after OT-I adoptive transfer at day 0; bar graphs show mean ± SEM; data are representative of at least two independent experiments, each with at least three biological replicates per group for B–O, and with at least five biological replicates per group for A and P. **P < 0.01, *P < 0.05, ns = no significance by Student's *t* test or Mann–Whitney *U* test or unpaired *t* tests.

to assess whether similar deficiencies in the early establishment of key antitumor immune cells occurred here, without the confounding variable of tumor regression (Fig. 4 E). Following the reporter expression patterns, in both the late and early depletion settings, there was a significant and large depletion of the CD206$^+$ TAMs (Fig. 4, F and J). Importantly, there was once again an indirect loss of cDC1s and CD8 T cells (but not NK cells) specifically in the early but not the late depletion regimen (Fig. 4, G, H, K, and L), consistent with our results in the B78chOVA model. Likewise, no change was detected in overall cDC2 abundance (Fig. S3, N–P) with both early and late DTx treatment, although the fraction of CD206$^+$ cDC2s was reduced (Fig. 4, I and M). Some differences were observed with the B78chOVA model, including overall maintenance of TAM abundance in late (Fig. S3 O) despite robust depletion of the CD206$^+$ populations (Fig. 4 F). Other variations in compensatory populations, namely neutrophil enrichment in both regimens (albeit with much lower effect size in late depletion; Fig. S3, O and P) were observed. When evaluated further by directly measuring the total number of cells per gram of tumor, we observed that the early direct depletion of CD206$^+$ TAMs led to an indirect increase in neutrophils and the indirect loss of cDC1s and CD8 T cells, but not NK cells (Fig. S3 Q) in MC38chOVA tumors. Once again, this loss of lymphocytes was specific to the tumor and did not affect the CD8 T cell and NK cell numbers in the corresponding tdLN (Fig. S3 R).

Further, we found a (~75%) decrease in CXCL9-expressing TAMs in the early depletion condition (Fig. 4 N) and a large (~80%) reduction in C1q TAMs, which are the TAMs expressing the highest levels of CD206 (Fig. 4 O). With confirmation of key direct and indirect effects of CD206$^+$ TAM depletion in the MC38chOVA model, we treated subcutaneous MC38chOVA tumors in WT and DTR mice with OT-Is with concomitant early DTx administration. With the prediction that depletion of CD206$^+$ TAMs would thwart the tumor control ability of OT-Is, we tracked changes in tumor size and indeed observed significantly reduced OT-I–mediated tumor control of MC38chOVA tumors (Fig. 4 P) in the DTR group. These results demonstrate in a second tumor model the disruption of a key cDC1-centered antitumor module when CXCL9-producing CD206$^+$ TAMs were eliminated during its establishment, leading to the attenuation of CD8 T cell–mediated tumor control.

CD206$^+$ Mono/Mac signatures associate with antitumor immunity in human cancers

The data presented thus far provided substantial evidence of a context in which CD206$^+$ populations of Mono/Macs were in fact positive contributors to reactive antitumor immunity in mice rather than being simply immunosuppressive. Consistent with this understanding, we found that higher levels of *MRC1* RNA alone correlated with slightly better rather than worse survival from patient data in a large cohort curated from The Cancer Genome Atlas (TCGA) (Combes et al., 2022) (Fig. 5 A). We also sought to determine whether the revealed relationships between CD206$^+$ TAMs, CXCL9, and the cDC1:CD8:NK module in our study might similarly extend to human disease. To do so, we first applied differential gene expression (DGE) analysis of the Ctrl versus DTx-treated Mono/Mac populations (Fig. 5, B and C) (excluding neutrophils, cDC1, cDC2, and lymphocyte subsets) from our scRNASeq dataset (Fig. 3 B). We then used the top 10 differentially expressed genes (DEGs; by average log fold change and having an adjusted P value <0.01) to create CD206 "Replete" and "Depleted" gene signatures (Fig. 5 D). The former are DEGs associated with the presence of CD206$^+$ populations and not only included *C1qa*, *Cxcl9*, *Apoe*, but also several MHC-II related genes (Fig. 5, D and E), consistent with flow cytometry data on C1q TAM, CD206, CXCL9, and MHC-II expression described above. The Depleted signature contains genes differentially expressed in macrophages that remain after CD206$^+$ Mono/Mac depletion and included *Il1b*, *S100a8*, along with *Spp1* (Fig. 5, D and E). Even though we obtained these gene signatures based upon depletion of Mono/Macs using the prominent "M2" marker CD206, both M1- and M2-associated genes were differentially upregulated in Replete signature (Fig. 5 D), reiterating the lack of coordination among such markers when studied in vivo.

Using these signatures, we queried a previously described immune compartment-specific bulk RNASeq data derived from sorted HLA-DR$^+$ myeloid (to capture Mono/Macs and dendritic cells [DCs]), T, and total live cells from >200 human tumor biopsies (Combes et al., 2022) (Fig. 5, F and G) belonging to five common solid tumor indications (CRC: colorectal cancer, GYN: gynecological cancer, HNSC: head and neck squamous cell carcinoma, KID: kidney cancer; LUNG: lung carcinoma). Given our finding that the CD206$^+$ CXCL9-expressing TAMs recruit CXCR3-expressing cDC1-supportive lymphocytes, we predicted that the CD206 "Replete" but not the "Depleted" signature in the myeloid compartment would associate with previously established CD8, NK, and stimulatory cDC1s (stimulatory DC, or SDC) gene signatures (Broz et al., 2014; Combes et al., 2022). Indeed, the Replete signature, but not the Depleted signature, correlated significantly with those of each component of the tumor-reactive immune module (Fig. 5 F) of SDCs (Fig. 5 G), CD8 T cells (Fig. 5 H), and NK cells (Fig. S3). Given that it is by now

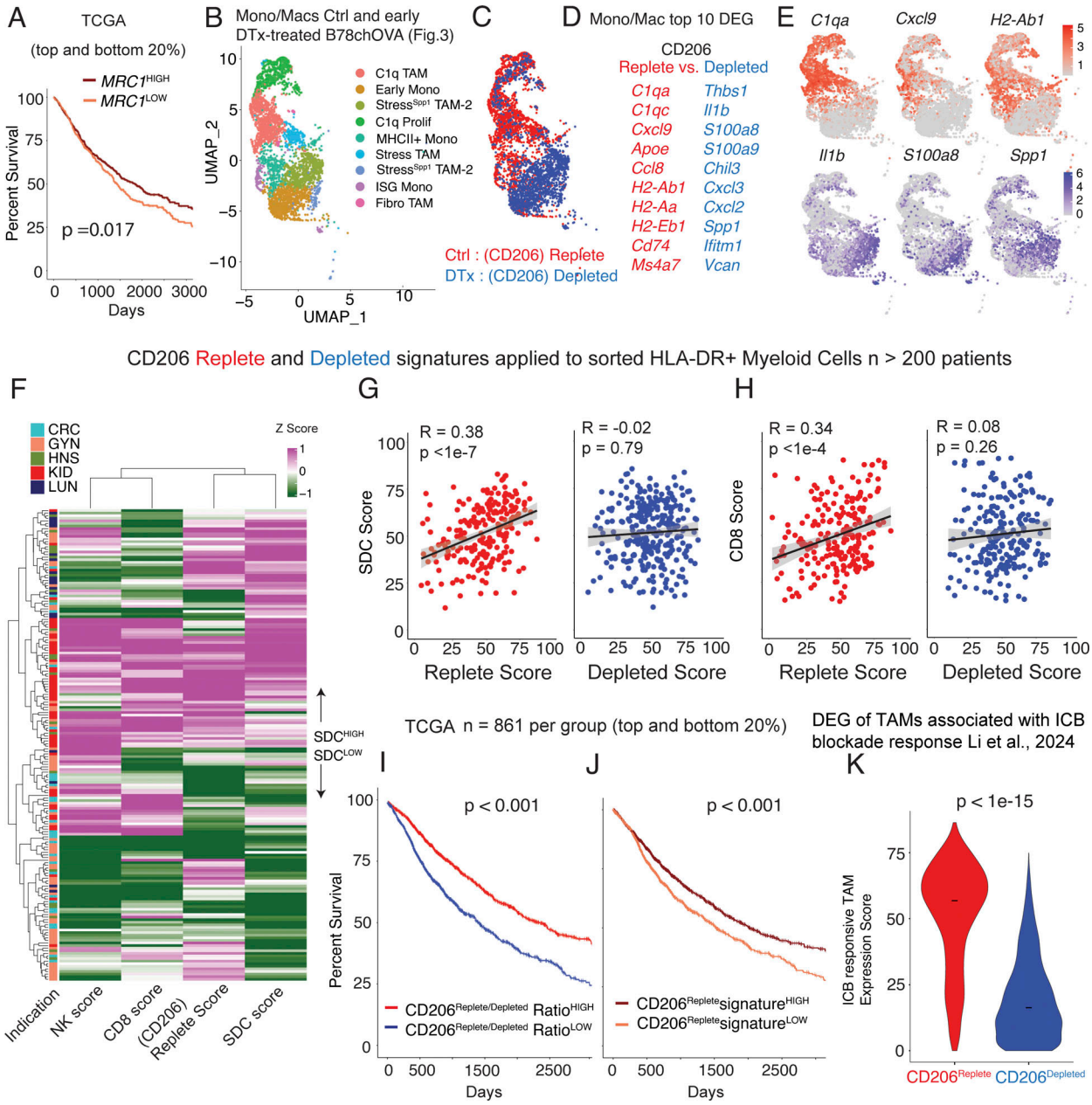

Figure 5. **CD206^{Replete} Mono/Mac signature associates with antitumor immunity in human cancers. (A)** Kaplan–Meier survival curves of patients in TCGA grouped by the expression of *MRC1* gene. **(B and C)** (B) UMAP representation of the Mono/Mac subsets and (C) overlay of the CD206 Replete (Ctrl) and depleted (DTx) groups on the UMAP from spatial scSeq described in Fig. 3. **(D)** Top 10 genes from DGE of Mono/Macs in the Ctrl versus DTx treated conditions, which were used to generate CD206 Replete and CD206 Depleted Mono/Mac signature scores. **(E)** Expression of select genes defining the CD206 replete (*C1qa*, *Cxcl9*, *H2-Ab1*) and the CD206 depleted (*Il1b*, *S100a8*, *Spp1*) signatures overlaid on the same UMAP. **(F)** Heatmap of z-scored CD206^{Replete}, CD8, NK, and SDC score, calculated from sorted immune and live compartments, as previously described (Combes et al., 2022) in colorectal (CRC), gynecological (GYN), head and neck (HNS), kidney (KID), and lung (LUN) cancer patients. **(G and H)** Scatter plots of the myeloid-specific CD206 Replete and Depleted score per patient with the (G) SDC score and (H) CD8 T cell score (Pearson R and P value for the null hypothesis that there is not a correlation are noted). **(I and J)** Kaplan-Meier survival curves of patients grouped by the value of the (I) CD206^{Replete}:CD206^{Depleted} signature ratio and (J) CD206^{Replete} signature in TCGA. **(K)** Expression score for TAMs associated with ICB responsiveness derived from Li et al. (2024) in the CD206^{Replete} versus CD206^{Depleted} Mono/Macs; *n* = 205 patients in G and H; and *n* = 861 patients per group in I and J; P values for the log-rank test are noted in A, I, and J, and that for the Wilcoxon test is shown in K.

well-established that SDCs are associated with survival (Broz et al., 2014), we also queried whether the relative abundance of CD206 Replete Mono/Macs (i.e., CD206^{Replete}/CD206^{Depleted} ratio) was correlated with better survival in patients. In the TCGA dataset, we observed a large (~20% in 5-year survival) and significant shift in survival for patients biased toward the CD206^{Replete} Mono/Mac signature (Fig. 5 I). Indeed, patients scoring high on the CD206^{Replete} Mono/Mac signature alone were also found to have significantly better survival but with a reduced effect size (Fig. 5 J) as compared with the ratio. Among

specific indications, the Replete/Depleted signature ratio was associated with overall survival in lung, liver, pancreatic, bladder, kidney cancer, and melanoma (Fig. S3 T). To further test whether CD206^{Replete} Mono/Macs are important for ICB responsiveness, we used a very recently published atlas of tumor-infiltrating myeloid cells from human patients, which identifies a subset of ApoE-expressing TAMs associated with ICB responsiveness (Li et al., 2024). Using the top 10 DEGs (by log fold change, filtered by adjusted P value <0.01) of this TAM cluster, which included *C1QA*, *C1QB,* and *CXCL9*, we found this signature score for ICB-responsive TAMs to be significantly higher in the CD206^{Replete} versus CD206^{Depleted} Mono/Macs in our data (Fig. 5 K). Thus, contrary to the simplistic labeling of CD206-expressing macrophages as immunosuppressive, this data establishes contexts in which these Mono/Macs are a critical organizing fulcrum for the reactive module of antitumor immunity. Taken together, these data contribute to a nuanced understanding of the context-dependent role of TAMs in the TME, necessary to rationally design next-generation myeloid-targeting immunotherapies in cancer.

Revealed relationships between CD206^{+} TAMs, antitumor immunity, and macrophage targeting in tumors

cDC1s have been previously linked to FLT3L and XCL1-producing NK cells and activated CD8 T cells (Barry et al., 2018; Böttcher et al., 2018), and this network represents one module of immunity that predisposes to ICB response (reviewed in Im et al. [2021]). The same CD8 T cells in turn may be recruited and expanded by chemokines and antigen presentation by cDC1s, creating a virtuous feedback loop for antitumor immunity. It was, however, previously unexplored how specific macrophage subsets support or thwart this antitumor archetype. Here, we demonstrate that CD206 expression in macrophages is robustly correlated with their expression of CXCL9, and these macrophages play a critical role in establishing the cDC1:NK-CD8 antitumor reactive module in tumors.

This work is the latest in a series of publications (Azizi et al., 2018; Bill et al., 2023; Ginhoux et al., 2016; Mujal et al., 2022; Zheng et al., 2021) that force re-evaluation of the prevalent but insufficient M1/M2 classification of macrophages in tumors. Notably, CD206 expression is still often used to categorize macrophages as immunosuppressive and "M2-like," even though strong in vivo data supporting this assertion is lacking. Here, we show that CD206 should not be used as an unqualified indicator of immunosuppressive function. Indeed, in the context of ongoing antitumor responses studied here in the early depletion setting, these TAMs are crucial for the effective recruitment of critical immune cells.

When thinking about these revealed functions of TAMs expressing CD206, we also note that this study specifically found them critical in early T cell recruitment. Previous work has highlighted the antigen-presentation capabilities of CD206^{+} macrophages (Modak et al., 2022). However, direct analyses of antigen-dependent interactions of CD8 T cells with mature TAMs (which are biased for those that express CD206) show that they more often promote T cell exhaustion (Kersten et al., 2022; Nixon et al., 2022). Thus, TAMs may have distinct phenotypes and functions depending on the immunological state of the tumor—perhaps reflected in the early and late depletion conditions shown here. Future studies to understand this balance of pro- and antitumor effects of TAMs are critical. At present, one should not simplistically take our study to indicate that CD206^{+} macrophages are universally favorable for antitumor immunity. However, the M1/M2 dichotomy—and particularly a version that equates CD206 with pro-tumoral functions—appears to be a misleading lens through which to view macrophage functional heterogeneity.

Other recent data using *CXCL9* versus *SPP1* gene expression to functionally classify macrophages in human tumors (Bill et al., 2023) as anti- or pro-tumor respectively, are aligned with our findings. In our earlier studies of *SPP1* in macrophages (Mujal et al., 2022), these were observed in human tumors, likely embedded within an Arg1 (Stress) TAM subset in mice, and here they only emerged as a distinct cluster due to their disproportionate enrichment post depletion. As we have previously noted (Mujal et al., 2022), "Stress" macrophages are distinctly glycolytic, express *Hif1α*, and are likely the cells that have previously been defined as hypoxic macrophages (Bosco et al., 2006; White et al., 2004) and now associated with poor patient outcomes. In our model, these SPP1 TAMs appear to be orthogonal to the *C1q*, *Apoe*-expressing CD206^{hi} mature TAMs (also VCAM1 expressing, used to gate on these cells by flow cytometry) expressing CXCL9, dominant in the CD206^{Depleted} and CD206^{Replete} conditions, respectively. As such, the origins of this increased SPP1 subset, perhaps from bone marrow–derived monocyte precursors, warrant further investigation. In this context, slow and spontaneously growing autochthonous tumors are an important tool for such kinetic studies. Individually, parts of this disrupted antitumor axis including macrophage-specific CXCL9/10 expression in isolation (House et al., 2020; Qu et al., 2020) or as opposed to SPP1 expression (Bill et al., 2023), and the presence of cDC1, NK cells, and antigen-specific CD8 T cells (Barry et al., 2018; Böttcher et al., 2018) have been associated with ICB responses. This is consistent with our analysis of recently published data on ICB-responsive TAMs (Fig. 5 K) and suggests that targeting CD206^{+} TAMs in therapeutic contexts of mobilization of CD8 T cells from lymph nodes may preclude antitumor efficacy of those therapies.

Studies prior to ours and using more universal Mono/Mac depletion have also variably reported compensatory neutrophil influx when depleting cells of monocytic origin in tumors (Kumar et al., 2017; O'Brien et al., 2021; Ries et al., 2014). Our data also shows an increase in neutrophils in the early CD206-gated depletion condition but a lack of similar influx in the late depletion regimen. One interpretation of our data is that a microenvironment-dependent opportunistic filling of the early myeloid niche by neutrophils takes place in the absence of sufficient Mono/Macs and the reactive immune components. While further studies may uncover key nodes of this balance of myeloid populations, our results show that the compensatory neutrophils do not contribute to the reduction of CXCR3-dependent lymphocyte recruitment (House et al., 2020), which is the primary driver leading to the loss of the key tumor-reactive archetype.

One key success of our study is the ability to differentially visualize and target subsets of TAMs within the TME. By microscopy, the localization of Venus$^+$ macrophages was consistent with previous studies, which showed presence at the tumor edge, including those that attribute immune cell exclusion to these cells at the margin (Peranzoni et al., 2018; Yofe et al., 2023). The differences in tumor models, phenotype, and time-dependent function of the targeted macrophage subsets may explain the different functions attributed to apparently similar cell populations. Many questions regarding the specific role of TAMs have remained obscured or unanswered partly owing to the lack of sufficiently specific and penetrant tools to manipulate them in vivo. Commonly used methods, while important and useful, lack sufficient specificity, including the depletion of all monocytes and monocyte-derived DCs (CSF1R blocking antibody; Greter et al., 2012; Naik et al., 2015; Swierczak et al., 2014) and the depletion of all phagocytic cells and the arrest of neutrophils (Clodronate; Culemann et al., 2023). In this context, the novel conditional CD206 reporter introduced here—paired with *Csf1r*-Cre to avoid depleting other non-myeloid cells that express CD206—provides a more selective marking and depletion tool for CD206$^+$ TAMs, with a further potential to target various subpopulations by altering the Cre driver alleles.

Overall, our results indicate that even this subset-dependent depletion of Mono/Mac populations may not be prudent in all contexts. To this extent, while anti-CSF1R antibodies have failed to show benefits in clinical trials (Gomez-Roca et al., 2019), other modified strategies (Klemm et al., 2021) or drugs that modulate specific subsets (Juric et al., 2023) may prove more surgical. Systematically dissecting the role of individual TAM subtypes will continue to be crucial to deciphering their context-dependent and complex roles in the TME with a view toward harnessing them for better immunotherapy outcomes.

Materials and methods

Mice

All mice were treated in accordance with the regulatory standards of the National Institutes of Health and American Association of Laboratory Animal Care and were approved by the University of California, San Francisco (UCSF) Institutional Animal Care and Use Committee (IACUC). *Mrc1*(CD206)$^{\text{LSL-Venus-DTR}}$ mice in the C57BL6/J background were custom-generated from Biocytogen Inc. and then maintained at the UCSF Animal Barrier facility under specific pathogen–free conditions. C57BL6/J, C57BL6/J CD45.1 (B6.SJL-Ptprc^a Pepc^b/BoyJ), OT-I (C57BL/6-Tg(TcraTcrb)1100Mjb/J), Csf1r$^{\text{Cre}}$ (C57BL/6-Tg(Csf1r-cre)1Mnz/J), and LysM$^{\text{Cre}}$ (B6.129P2-*Lyz2*$^{tm1(cre)Ifo}$/J) mice were purchased for use from Jackson Laboratories and maintained in the same facility in the C57BL6/J background. For adoptive transfer experiments, CD45.1$^{\text{het}}$; OT-I$^{\text{het}}$ (denoted simply as CD45.1; OT1) mice were used. Mice of either sex ranging in age from 6 to 14 wk were used for experimentation.

Depletion of select immune cell populations

For depletion of CD206-expressing macrophages, 500 ng (20 ng/g body weight, assuming an average 25 g weight for each mouse) DTx (List Biological Laboratories) in 100 µl 1× PBS was injected intraperitoneally into each mouse—for both *Csf1r*$^{\text{Cre}}$; *Mrc1*(CD206)$^{\text{LSL-Venus-DTR}}$ (DTR) or alternately *LysM*$^{\text{Cre}}$; *Mrc1*(CD206)$^{\text{LSL-Venus-DTR}}$ (DTR^L) and *Mrc1*(CD206)$^{\text{LSL-Venus-DTR}}$ (WT) groups—at every time point. For the early depletion regimen, injections were started 2 days after the adoptive transfer of T cells and continued every 2–3 days till the endpoint, while for the late depletion regime, injections began at day 10 after T cell injection and continued till the endpoint. For testing the effects of DTx in tumor-free tissue, a similar dosing of DTx as the early depletion regime was implemented without tumor injection, and the skin (ectopic tumor site) was isolated for analysis. Mice were found to be healthy and without frank health issues with six doses of 500 ng DTx (early depletion regime), but were monitored nevertheless throughout the experiment, as per IACUC guidelines.

For depletion of neutrophils, mice were treated with 200 µg/dose of anti-Ly6G antibody (Clone 1A8; BioXCell) in PBS intraperitoneally every 2–3 days starting one dose after the beginning of DTx treatment and coincident with DTx treatment thereafter. Control mice were similarly treated with the corresponding isotype control antibody at the same dose (Clone 2A3; BioXCell).

Mouse tumor digestion and flow cytometry

Tumors from mice were processed to generate single-cell suspensions as described previously (Barry et al., 2018). Briefly, tumors were isolated and mechanically minced on ice using razor blades, followed by enzymatic digestion with 200 µg/ml DNAse (Sigma-Aldrich), 100 U/ml Collagenase I (Worthington Biochemical), and 500 U/ml Collagenase IV (Worthington Biochemical) for 30 min at 37°C while shaking. Digestion was quenched by adding excess 1× PBS, filtered through a 100-µm mesh, spun down, and red blood cells were removed by incubating with RBC lysis buffer (155 mM NH_4Cl, 12 mM $NaHCO_3$, 0.1 mM EDTA) at room temperature for 10 min. The lysis was quenched with excess 1× PBS, spun down, and resuspended in FACS buffer (2 mM EDTA + 1% FCS in 1× PBS) to obtain single-cell suspensions. For counting absolute numbers of cells, CountBright Absolute Counting Beads (Thermo Fisher Scientific) were added to the cell suspensions prior to staining, while noting the total weight of the tumor and the fraction of the total tumor cell digest used for staining.

For each sample, 2.5–3 million cells/sample were stained in a total of 50 µl of antibody mixture for flow cytometry. Cells were first stained with Zombie NIR Fixable live/dead dye (1:500) (Biolegend) for 20 min at 4°C. Next, cells were washed in FACS buffer followed by surface staining for 30 min at 4°C with directly conjugated antibodies diluted in FACS buffer containing 1:100 anti-CD16/32 (Fc block; BioXCell) to block non-specific binding. Antibody dilutions ranged from 1:100–1:400, optimized separately. After surface staining, cells were washed again with FACS buffer. For intracellular staining, cells were fixed for 20 min at room temperature using the IC Fixation Buffer (BD Biosciences) and washed in permeabilization buffer from the FoxP3 Fix/Perm Kit (BD Biosciences). Antibodies against intracellular targets were diluted in permeabilization buffer containing 1:100 Fc Block (same as above), and cells were

incubated for 30 min at 4°C followed by another wash prior to readout on a BD LSRII or Fortessa Cytometer.

Processing and flow cytometry analysis of other mouse organs

To phenotype cells from lymphoid organs, inguinal, axillary, and brachial (tumor-draining) lymph nodes were isolated, pried open with tweezers (lymph nodes) or cut into small pieces (spleen), and digested with the same digestion cocktail as above, intermittently pipetting with cut P1000 pipette tips to enhance mechanical digestion. The resulting suspensions were then filtered using a 100-µm filter, washed with 1× PBS, spun down, and resuspended in FACS buffer to generate single-cell suspensions, ready for staining.

Skin digestion was done as previously described (Ruhland et al., 2020). Briefly, mice were shaved and depilated (using Nair) prior to the removal of dorsal skin. The skin was then rid of fat and minced with scissors and a razor blade in the presence of 1 ml of digest media (2 mg/ml collagenase IV [Roche], 1 mg/ml hyaluronidase [Worthington], and 0.1 mg/ml DNase I [Roche] in RPMI-1640 [GIBCO]). The minced skin was then moved to a 50 ml conical with 5 ml additional digest solution and incubated at 37°C for 45 min with shaking and intermittent vortexing before being washed and passed through a 70-µm strainer prior to staining.

Analysis of flow cytometry data was done on FlowJo and later plotted on GraphPad Prism or R. Relative mean fluorescence intensity (MFI) of the Venus reporter was calculated by subtracting the background average MFI of the same channel in WT samples from those in each DTR sample.

Tumor injections and adoptive transfer of CD8 T cells into tumors

The B78chOVA and MC38chOVA cancer cell lines, as previously described (Barry et al., 2018; Kersten et al., 2022), were generated by incorporating the same mCherry-OVA construct used to establish the PyMTchOVA spontaneous mouse line (Engelhardt et al., 2012). For tumor injections, the corresponding cells were grown to near confluency (cultured in DMEM with 10% FCS [Benchmark] and 1% PSG [Penicillin/Streptomycin/Glutamine; Gibco]) and harvested using 0.05% Trypsin-EDTA (Gibco) and washed 3× with PBS (Gibco). The number of cells to be injected per mouse was resuspended in PBS to a final volume of 50 µl per injection. The suspension was injected subcutaneously into the flanks of anesthetized and shaved mice. Tumors were allowed to grow for 14–21 days unless otherwise noted before tumors and tdLN were harvested for analysis. CD8 T cells were isolated from CD45.1;OT-1 mice using the EasySep Negative Selection Kit (Stem Cell Bio), resuspended in 1× PBS, and 100 µl was injected into each tumor-bearing mouse. 1 million CD8 T cells were injected retro-orbitally into each mouse 5 days after tumor injection. Tumor measurements were done by measuring the longest dimension (length) and approximately perpendicular dimension (width) using digital calipers, rounded to one decimal place each. For experiments using the PyMTchOVA strain, mammary tumor-bearing females in the age range of 15–24 wk were used when mice developed at least two palpable tumors.

Spatial scRNASeq and analysis

Spatial scSeq of immune cell populations at the tumor edge, interface, and interior zones was performed using ZipSeq, as previously described (Kersten et al., 2022), with the additional condition of DTx treatment integrated into the dataset. From visualizing several tumors, we designated the collagen-rich region ∼300 µm from the tumor boundary as the "edge," contiguous ∼300 µm region as the interfacial "mid," and the rest as the interior region. When imaging on the customized Zeiss Axiovert 200M inverted microscope fitted with a Mosaic DMD (Andor), the outer boundaries of the tumors were determined by autofluorescence. For representative capture of the regions at high resolution, serial slices were imaged by a custom two-photon microscope, corresponding to the data shown in Fig. 3 A. Briefly, B78chOVA tumors subcutaneously grown in $Csf1r^{Cre}$; $Mrc1^{LSL\text{-}Venus\text{-}DTR}$ mice on day 12 after adoptive transfer of 1 million CD2dsRed; OT-I CD8 T cells with (DTx) and without (Control) DTx treatment (early depletion regime) were harvested and sliced into 160-µm slices using a Compressotome (VFZ-310-0Z; Precisionary Instruments). Imaging, spatial barcoding, subsequent digestion, sorting, encapsulation (10X Genomics) and library construction, CellRanger processing, and alignment were performed as described previously (Hu et al., 2020; Kersten et al., 2022). The two separate sequencing runs (Control and DTx) were assembled and integrated into a single data structure using Harmony (Korsunsky et al., 2019). The final object underwent scaling and then scoring for cell cycle signatures (S and G2M scores as computed using Seurat's built-in CellCycleScoring function). The object then underwent regression for cell cycle effects (S and G2M score as described in the Seurat vignette) and percent mitochondrial reads before principal component analysis (PCA).

Relative abundance from scSeq data was calculated as follows: $\log_2$ (% of each cluster [cell type] within a tumor region (Edge, Mid, Inner) in the Ctrl/(% of the same cluster in the same region in the DTx treated group), thereby yielding positive values for depletion and negative values for enrichment. While abundances were calculated with the broad clusters from the overall object, the lymphoid clusters were isolated to a separate object and reclustered to further probe for individual gene expression (*Cxcr3*, *Flt3l*, *Xcl1*) in the resulting subsets.

Transwell assay of CD8 T cell migration

For transwell assays, subcutaneously injected B78chOVA tumors were grown for 14 days and then harvested, digested, and sorted by fluorescence-activated cell sorting (FACS) for $CD206^+$ versus $CD206^-$ TAMs (gating scheme as in Fig. S1 A). 3 days before the sort, CD8 T cells from a B6 mouse were harvested and stimulated in vitro with anti-CD3/anti-CD28 Dynabeads (Thermo Fisher Scientific) for 24 h, taken off the beads, and rested in 10 U/ml IL-2 for an additional 48 h to produce effector-like CD8 T cells. After the sort, 500,000 activated T cells were plated in 75 µl T cell media (RPMI + 10% FCS + 50 µM β-mercaptoethanol) on top of a 5-µm transwell insert (Corning), allowed to settle for 30 mins and subsequently, 10,000 sorted $CD206^-$, $CD206^+$ TAMs or no TAMs were added to the bottom well to induce T cell migration. Cells at the bottom were collected at 3 h, mixed with

CountBright absolute counting beads, stained, and analyzed by flow cytometry to quantify the number of CD8 T cells migrated. The total number of CD8 T cells migrated in each condition was normalized to the average number of cells migrated in the no TAM condition.

Human tumor samples

All tumor samples were collected with patient consent after surgical resection under a UCSF Institutional Review Board (IRB)-approved protocol (UCSF IRB# 20-31740) as part of the UCSF Immunoprofiler project, as described previously (Combes et al., 2022). In brief, freshly resected samples were transported in ice-cold DPBS or Leibovitz's L-15 medium before digestion and processing to generate a single-cell suspension. The five most well-represented cancer indications in this collection were included in the cohort: colorectal cancer (CRC), gynecological cancers (GYN), head and neck cancer (HNSC), kidney cancer (KID), and lung cancer (LUNG).

Transcriptomic analysis of human tumors

Briefly, tumor samples were thoroughly minced with surgical scissors and transferred to GentleMACS Tubes containing 800 U/ml Collagenase IV and 0.1 mg/ml DNase I in L-15/2% FCS per 0.3 g tissue. GentleMACS tubes were then installed onto the GentleMACS Octo Dissociator (Miltenyi Biotec) and incubated for 20 min (lymph node) or 35 min (tumor) according to the manufacturer's instructions. Samples were then quenched with 15 ml of sort buffer (PBS/2% FCS/2 mM EDTA), filtered through 100-µm filters, and spun down. Red blood cell lysis was performed with 175 mM ammonium chloride, if needed. Freshly digested tumor samples were sorted by FACS into the conventional T cell, regulatory T cell, myeloid, tumor, and in some cases, stromal compartments, and bulk RNASeq was performed on sorted cell fractions. mRNA was isolated from sorted fractions and libraries were prepared using Illumina Nextera XT DNA Library Prep kit. The libraries were sequenced using 100 bp paired-end sequencing on HiSeq4000. The sequencing reads we aligned to the Ensembl GRCh38.85 transcriptome build using STAR (Dobin et al., 2013) and gene expression was computed using RSEM (Li and Dewey, 2011). Sequencing quality was evaluated in-house by the Eisenberg housekeeping (EHK) score, where each sample was assigned a score of 0 through 10 based on the number of EHK genes that were expressed above a precalculated minimum threshold. The threshold was learned from our data by examining the expression distributions of EHK genes and validated using the corresponding distributions in TCGA. A score of 10 represented the highest quality data where 10 out of 10 EHK genes are expressed above the minimum threshold. The samples used here for gene expression analyses had an EHK score of ≥7 to ensure data quality. Ensemble gene signature scores were calculated by converting the expression of each gene in the signature to a percentile rank among all genes and then determining the mean rank of all the genes in the signature (Ray et al., 2023, *Preprint*), modified from Combes et al. (2022). The corresponding gene lists for obtaining CD8 T cell (Combes et al., 2022), NK (Barry et al., 2018), and the SDC score (Broz et al., 2014) are as described in these previous works.

Analyses of public or published datasets

Survival analyses using the TCGA dataset were performed using the TCGA sub-cohort described in Combes et al. (2022). Briefly, tumor RNASeq counts and TPM along with curated clinical data for 13 cancer types (bladder cancer [BLCA], colon adenocarcinoma [COAD], glioblastoma [GBM], gynecological cancer [GYN] [grouping ovarian cancer [OV], uterine corpus endometrial carcinoma [UCEC], and uterine carcinosarcoma [UCS]], head and neck squamous cell carcinoma [HNSC], kidney renal clear cell carcinoma [KIRC], liver hepatocellular carcinoma [LIHC], lung adenocarcinoma [LUAD], pancreatic adenocarcinoma [PAAD], sarcoma [SARC], and skin cutaneous melanoma [SKCM]) were filtered down to include primary solid tumors and metastatic samples only, to parallel the cohort samples in UCSF Immunoprofiler (Combes et al., 2022). This resulted in a TCGA sample set of 4,341 tumors. $CD206^{Replete}$ gene scores were generated by first normalizing (using percentiles) the expression values of each gene composing the signature across all patients, followed by averaging these normalized values for each patient. The same method was used for deriving $CD206^{Depleted}$ gene scores, and we then calculated the ratio of $CD206^{Replete}/CD206^{Depleted}$ gene scores by dividing corresponding score values for each patient. For survival analysis, patients were split into either $CD206^{Replete}$ gene score ^{HIGH} versus ^{LOW} (top/bottom 20% respectively, n = 861) or $(CD206^{Replete}:CD206^{Depleted}$ gene signature ratio$)^{HIGH}$ versus $(CD206^{Replete}:CD206^{Depleted}$ gene signature ratio$)^{LOW}$ (top/bottom 20% respectively, n = 861) and analyzed using a log-rank test.

To obtain gene signatures of tumor-infiltrating macrophages associated with ICB response, DEGs from the response-associated "Macro_FOLR2$^+$APOE$^+$" cluster (Li et al., 2024) were filtered by adjusted P value <0.01 and arranged by decreasing average log fold change of expression. From this list, the murine orthologs of the top 10 genes that were also occurring in our spatial scSeq dataset (thereby excluding *Ccl18* and *Sds*) were obtained as follows: *Gpnmb*, *Plau*, *Cxcl9*, *Nr1h3*, *Lgmn*, *Ccl4*, *Acp5*, *C1qb*, *Rgs1*, and *C1qa*. The ensemble gene expression score for this signature was generated using the percentile rank method as mentioned above.

Two-photon imaging of tumor slices

Tumor slices (adjacent to the ones used for spatial barcoding by ZipSeq) were fixed in 2% paraformaldehyde (Sigma-Aldrich), washed, and left overnight in 1× PBS at 4°C before imaging on a custom-made two-photon microscope, as previously described (Broz et al., 2014), to visualize the Venus reporter and CD2dsRed marked CD8 T cells and fibrous collagen by second harmonic generation (SHG). Dual laser excitations at 800 and 950 nm were used to excite the requisite fluorophores and capture those emissions and SHG in non-overlapping detection channels.

Statistical analysis

Statistical analysis was done in GraphPad Prism or in R. For testing the null hypothesis between two groups, Student's t tests and or the non-parametric Mann–Whitney U tests or Wilcoxon rank-sum test was used depending on the number and distribution of data points. Likewise, for testing null hypotheses among three or more groups, ANOVA or non-parametric tests were performed, followed by post-hoc test, correcting for false

discovery rates (threshold = 0.05) in multiple comparisons. Log-rank test was used for null hypothesis testing in survival data. Unless otherwise mentioned, data are representative of at least two independent experiments.

Online supplemental material

Fig. S1 shows a flow cytometry gating scheme to identify various immune cells in tumors and tdLN and reporter expression in different contexts. Fig. S2 shows intratumoral immune compositions and an abundance of specific subsets with various perturbations in B78chOVA. Fig. S3 includes gene expression supporting scSeq cluster identification and chemokine expression patterns; it shows reporter expression in MC38chOVA and immune compositions with DTx-mediated depletion in the same, and further data associating CD206$^+$ Mono/Macs with antitumor immunity in human cancers.

Data availability

Sequencing data are available at GEO accession: GSE184398 associated with Combes et al. (2022), GEO accession: GSE201074 associated with Kersten et al. (2022) and GEO accession GSE281472 associated with this study. Other data and reagents will also be available upon reasonable request, please contact the authors directly.

Acknowledgments

We thank members of the Krummel lab for their input to the manuscript.

This work was supported by National Institutes of Health grants NIH R01CA197363 and NIH R37AI052116. A. Ray was supported by a Cancer Research Institute Postdoctoral Fellowship (CRI2940). K.H. Hu was supported by an American Cancer Society and Jean Perkins Foundation Postdoctoral Fellowship. N.F. Kuhn was supported by the Cancer Research Institute/Merck Postdoctoral Fellowship (CRI4546).

Author contributions: A. Ray: Conceptualization, Data curation, Formal analysis, Investigation, Methodology, Validation, Visualization, Writing - original draft, Writing - review & editing, K.H. Hu: Formal analysis, Investigation, Methodology, Software, Visualization, Writing - review & editing, K. Kersten: Conceptualization, Formal analysis, Investigation, Writing - review & editing, T. Courau: Formal analysis, Visualization, N.F. Kuhn: Methodology, Resources, I. Zaleta-Linares: Investigation, B. Samad: Data curation, Formal analysis, A.J. Combes: Methodology, Project administration, Resources, Writing - review & editing, M.F. Krummel: Conceptualization, Funding acquisition, Methodology, Project administration, Supervision, Visualization, Writing - original draft, Writing - review & editing.

Disclosures: A.J. Combes reported grants from Eli Lily, grants from Genentech, other from Foundery Innovations, and other from Survey Genomics outside the submitted work. No other disclosures were reported.

Submitted: 3 June 2024
Revised: 1 September 2024
Accepted: 30 October 2024

References

Azizi, E., A.J. Carr, G. Plitas, A.E. Cornish, C. Konopacki, S. Prabhakaran, J. Nainys, K. Wu, V. Kiseliovas, M. Setty, et al. 2018. Single-cell map of diverse immune phenotypes in the breast tumor microenvironment. *Cell*. 174:1293–1308.e36. https://doi.org/10.1016/j.cell.2018.05.060

Barry, K.C., J. Hsu, M.L. Broz, F.J. Cueto, M. Binnewies, A.J. Combes, A.E. Nelson, K. Loo, R. Kumar, M.D. Rosenblum, et al. 2018. A natural killer-dendritic cell axis defines checkpoint therapy-responsive tumor microenvironments. *Nat. Med.* 24:1178–1191. https://doi.org/10.1038/s41591-018-0085-8

Barry, S.T., D.I. Gabrilovich, O.J. Sansom, A.D. Campbell, and J.P. Morton. 2023. Therapeutic targeting of tumour myeloid cells. *Nat. Rev. Cancer*. 23:216–237. https://doi.org/10.1038/s41568-022-00546-2

Bill, R., P. Wirapati, M. Messemaker, W. Roh, B. Zitti, F. Duval, M. Kiss, J.C. Park, T.M. Saal, J. Hoelzl, et al. 2023. CXCL9:SPP1 macrophage polarity identifies a network of cellular programs that control human cancers. *Science*. 381:515–524. https://doi.org/10.1126/science.ade2292

Binnewies, M., E.W. Roberts, K. Kersten, V. Chan, D.F. Fearon, M. Merad, L.M. Coussens, D.I. Gabrilovich, S. Ostrand-Rosenberg, C.C. Hedrick, et al. 2018. Understanding the tumor immune microenvironment (TIME) for effective therapy. *Nat. Med.* 24:541–550. https://doi.org/10.1038/s41591-018-0014-x

Bosco, M.C., M. Puppo, C. Santangelo, L. Anfosso, U. Pfeffer, P. Fardin, F. Battaglia, and L. Varesio. 2006. Hypoxia modifies the transcriptome of primary human monocytes: Modulation of novel immune-related genes and identification of CC-chemokine ligand 20 as a new hypoxia-inducible gene. *J. Immunol.* 177:1941–1955. https://doi.org/10.4049/jimmunol.177.3.1941

Böttcher, J.P., E. Bonavita, P. Chakravarty, H. Blees, M. Cabeza-Cabrerizo, S. Sammicheli, N.C. Rogers, E. Sahai, S. Zelenay, and C. Reis e Sousa. 2018. NK cells stimulate recruitment of cDC1 into the tumor microenvironment promoting cancer immune control. *Cell*. 172:1022–1037.e14. https://doi.org/10.1016/j.cell.2018.01.004

Bourdely, P., G. Anselmi, K. Vaivode, R.N. Ramos, Y. Missolo-Koussou, S. Hidalgo, J. Tosselo, N. Nuñez, W. Richer, A. Vincent-Salomon, et al. 2020. Transcriptional and functional analysis of CD1c$^+$ human dendritic cells identifies a CD163$^+$ subset priming CD8$^+$CD103$^+$ T cells. *Immunity*. 53:335–352.e8. https://doi.org/10.1016/j.immuni.2020.06.002

Broz, M.L., M. Binnewies, B. Boldajipour, A.E. Nelson, J.L. Pollack, D.J. Erle, A. Barczak, M.D. Rosenblum, A. Daud, D.L. Barber, et al. 2014. Dissecting the tumor myeloid compartment reveals rare activating antigen-presenting cells critical for T cell immunity. *Cancer Cell*. 26:938. https://doi.org/10.1016/j.ccell.2014.11.010

Carmona-Fontaine, C., M. Deforet, L. Akkari, C.B. Thompson, J.A. Joyce, and J.B. Xavier. 2017. Metabolic origins of spatial organization in the tumor microenvironment. *Proc. Natl. Acad. Sci. USA*. 114:2934–2939. https://doi.org/10.1073/pnas.1700600114

Cheng, S., Z. Li, R. Gao, B. Xing, Y. Gao, Y. Yang, S. Qin, L. Zhang, H. Ouyang, P. Du, et al. 2021. A pan-cancer single-cell transcriptional atlas of tumor infiltrating myeloid cells. *Cell*. 184:792–809.e23. https://doi.org/10.1016/j.cell.2021.01.010

Chi, J.T., H.Y. Chang, G. Haraldsen, F.L. Jahnsen, O.G. Troyanskaya, D.S. Chang, Z. Wang, S.G. Rockson, M. van de Rijn, D. Botstein, and P.O. Brown. 2003. Endothelial cell diversity revealed by global expression profiling. *Proc. Natl. Acad. Sci. USA*. 100:10623–10628. https://doi.org/10.1073/pnas.1434429100

Combes, A.J., B. Samad, J. Tsui, N.W. Chew, P. Yan, G.C. Reeder, D. Kushnoor, A. Shen, B. Davidson, A.J. Barczak, et al. 2022. Discovering dominant tumor immune archetypes in a pan-cancer census. *Cell*. 185:184–203.e19. https://doi.org/10.1016/j.cell.2021.12.004

Culemann, S., K. Knab, M. Euler, A. Wegner, H. Garibagaoglu, J. Ackermann, K. Fischer, D. Kienhofer, G. Crainiciuc, J. Hahn, et al. 2023. Stunning of neutrophils accounts for the anti-inflammatory effects of clodronate liposomes. *J. Exp. Med.* 220:e20220525. https://doi.org/10.1084/jem.20220525

Dobin, A., C.A. Davis, F. Schlesinger, J. Drenkow, C. Zaleski, S. Jha, P. Batut, M. Chaisson, and T.R. Gingeras. 2013. STAR: Ultrafast universal RNA-seq aligner. *Bioinformatics*. 29:15–21. https://doi.org/10.1093/bioinformatics/bts635

Doedens, A.L., C. Stockmann, M.P. Rubinstein, D. Liao, N. Zhang, D.G. DeNardo, L.M. Coussens, M. Karin, A.W. Goldrath, and R.S. Johnson. 2010. Macrophage expression of hypoxia-inducible factor-1 alpha suppresses T-cell function and promotes tumor progression. *Cancer Res.* 70:7465–7475. https://doi.org/10.1158/0008-5472.CAN-10-1439

Dutertre, C.A., E. Becht, S.E. Irac, A. Khalilnezhad, V. Narang, S. Khalilnezhad, P.Y. Ng, L.L. van den Hoogen, J.Y. Leong, B. Lee, et al. 2019.

Single-cell analysis of human mononuclear phagocytes reveals subset-defining markers and identifies circulating inflammatory dendritic cells. *Immunity*. 51:573–589.e8. https://doi.org/10.1016/j.immuni.2019.08.008

Engelhardt, J.J., B. Boldajipour, P. Beemiller, P. Pandurangi, C. Sorensen, Z. Werb, M. Egeblad, and M.F. Krummel. 2012. Marginating dendritic cells of the tumor microenvironment cross-present tumor antigens and stably engage tumor-specific T cells. *Cancer Cell*. 21:402–417. https://doi.org/10.1016/j.ccr.2012.01.008

Ginhoux, F., J.L. Schultze, P.J. Murray, J. Ochando, and S.K. Biswas. 2016. New insights into the multidimensional concept of macrophage ontogeny, activation and function. *Nat. Immunol.* 17:34–40. https://doi.org/10.1038/ni.3324

Gomez-Roca, C.A., A. Italiano, C. Le Tourneau, P.A. Cassier, M. Toulmonde, S.P. D'Angelo, M. Campone, K.L. Weber, D. Loirat, M.A. Cannarile, et al. 2019. Phase I study of emactuzumab single agent or in combination with paclitaxel in patients with advanced/metastatic solid tumors reveals depletion of immunosuppressive M2-like macrophages. *Ann. Oncol.* 30:1381–1392. https://doi.org/10.1093/annonc/mdz163

Goswami, S., S. Anandhan, D. Raychaudhuri, and P. Sharma. 2023. Myeloid cell-targeted therapies for solid tumours. *Nat. Rev. Immunol.* 23:106–120. https://doi.org/10.1038/s41577-022-00737-w

Greter, M., J. Helft, A. Chow, D. Hashimoto, A. Mortha, J. Agudo-Cantero, M. Bogunovic, E.L. Gautier, J. Miller, M. Leboeuf, et al. 2012. GM-CSF controls nonlymphoid tissue dendritic cell homeostasis but is dispensable for the differentiation of inflammatory dendritic cells. *Immunity*. 36:1031–1046. https://doi.org/10.1016/j.immuni.2012.03.027

House, I.G., P. Savas, J. Lai, A.X.Y. Chen, A.J. Oliver, Z.L. Teo, K.L. Todd, M.A. Henderson, L. Giuffrida, E.V. Petley, et al. 2020. Macrophage-derived CXCL9 and CXCL10 are required for antitumor immune responses following immune checkpoint blockade. *Clin. Cancer Res.* 26:487–504. https://doi.org/10.1158/1078-0432.CCR-19-1868

Hu, K.H., J.P. Eichorst, C.S. McGinnis, D.M. Patterson, E.D. Chow, K. Kersten, S.C. Jameson, Z.J. Gartner, A.A. Rao, and M.F. Krummel. 2020. ZipSeq: Barcoding for real-time mapping of single cell transcriptomes. *Nat. Methods*. 17:833–843. https://doi.org/10.1038/s41592-020-0880-2

Hu, K.H., N.F. Kuhn, T. Courau, J. Tsui, B. Samad, P. Ha, J.R. Kratz, A.J. Combes, and M.F. Krummel. 2023. Transcriptional space-time mapping identifies concerted immune and stromal cell patterns and gene programs in wound healing and cancer. *Cell Stem Cell*. 30:885–903.e10. https://doi.org/10.1016/j.stem.2023.05.001

Im, K., A.J. Combes, M.H. Spitzer, A.T. Satpathy, and M.F. Krummel. 2021. Archetypes of checkpoint-responsive immunity. *Trends Immunol.* 42:960–974. https://doi.org/10.1016/j.it.2021.09.007

Juric, V., E. Mayes, M. Binnewies, T. Lee, P. Canaday, J.L. Pollack, J. Rudolph, X. Du, V.M. Liu, S. Dash, et al. 2023. TREM1 activation of myeloid cells promotes antitumor immunity. *Sci. Transl. Med.* 15:eadd9990. https://doi.org/10.1126/scitranslmed.add9990

Kersten, K., K.H. Hu, A.J. Combes, B. Samad, T. Harwin, A. Ray, A.A. Rao, E. Cai, K. Marchuk, J. Artichoker, et al. 2022. Spatiotemporal co-dependency between macrophages and exhausted CD8$^+$ T cells in cancer. *Cancer Cell*. 40:624–638.e9. https://doi.org/10.1016/j.ccell.2022.05.004

Klemm, F., A. Möckl, A. Salamero-Boix, T. Alekseeva, A. Schäffer, M. Schulz, K. Niesel, R.R. Maas, M. Groth, B.T. Elie, et al. 2021. Compensatory CSF2-driven macrophage activation promotes adaptive resistance to CSF1R inhibition in breast-to-brain metastasis. *Nat. Cancer*. 2:1086–1101. https://doi.org/10.1038/s43018-021-00254-0

Kodumudi, K.N., K. Woan, D.L. Gilvary, E. Sahakian, S. Wei, and J.Y. Djeu. 2010. A novel chemoimmunomodulating property of docetaxel: Suppression of myeloid-derived suppressor cells in tumor bearers. *Clin. Cancer Res.* 16:4583–4594. https://doi.org/10.1158/1078-0432.CCR-10-0733

Korsunsky, I., N. Millard, J. Fan, K. Slowikowski, F. Zhang, K. Wei, Y. Baglaenko, M. Brenner, P.R. Loh, and S. Raychaudhuri. 2019. Fast, sensitive and accurate integration of single-cell data with Harmony. *Nat. Methods*. 16:1289–1296. https://doi.org/10.1038/s41592-019-0619-0

Kowal, J., M. Kornete, and J.A. Joyce. 2019. Re-education of macrophages as a therapeutic strategy in cancer. *Immunotherapy*. 11:677–689. https://doi.org/10.2217/imt-2018-0156

Kumar, V., L. Donthireddy, D. Marvel, T. Condamine, F. Wang, S. Lavilla-Alonso, A. Hashimoto, P. Vonteddu, R. Behera, M.A. Goins, et al. 2017. Cancer-associated fibroblasts neutralize the anti-tumor effect of CSF1 receptor blockade by inducing PMN-MDSC infiltration of tumors. *Cancer Cell*. 32:654–668.e5. https://doi.org/10.1016/j.ccell.2017.10.005

Laviron, M., M. Petit, E. Weber-Delacroix, A.J. Combes, A.R. Arkal, S. Barthélémy, T. Courau, D.A. Hume, C. Combadière, M.F. Krummel, and A. Boissonnas. 2022. Tumor-associated macrophage heterogeneity is driven by tissue territories in breast cancer. *Cell Rep.* 39:110865. https://doi.org/10.1016/j.celrep.2022.110865

Li, B., and C.N. Dewey. 2011. RSEM: Accurate transcript quantification from RNA-seq data with or without a reference genome. *BMC Bioinformatics*. 12:323. https://doi.org/10.1186/1471-2105-12-323

Li, W., L. Pan, W. Hong, F. Ginhoux, X. Zhang, C. Xiao, and X. Li. 2024. A single-cell pan-cancer analysis to show the variability of tumor-infiltrating myeloid cells in immune checkpoint blockade. *Nat. Commun.* 15:6142. https://doi.org/10.1038/s41467-024-50478-8

Liu, Z., H. Wang, Z. Li, R.J. Dress, Y. Zhu, S. Zhang, D. De Feo, W.T. Kong, P. Cai, A. Shin, et al. 2023. Dendritic cell type 3 arises from Ly6C(+) monocyte-dendritic cell progenitors. *Immunity*. 56:1761–1777.e6. https://doi.org/10.1016/j.immuni.2023.07.001

Meiser, A., A. Mueller, E.L. Wise, E.M. McDonagh, S.J. Petit, N. Saran, P.C. Clark, T.J. Williams, and J.E. Pease. 2008. The chemokine receptor CXCR3 is degraded following internalization and is replenished at the cell surface by de novo synthesis of receptor. *J. Immunol.* 180:6713–6724. https://doi.org/10.4049/jimmunol.180.10.6713

Mitchem, J.B., D.J. Brennan, B.L. Knolhoff, B.A. Belt, Y. Zhu, D.E. Sanford, L. Belaygorod, D. Carpenter, L. Collins, D. Piwnica-Worms, et al. 2013. Targeting tumor-infiltrating macrophages decreases tumor-initiating cells, relieves immunosuppression, and improves chemotherapeutic responses. *Cancer Res.* 73:1128–1141. https://doi.org/10.1158/0008-5472.CAN-12-2731

Modak, M., A.K. Mattes, D. Reiss, W. Skronska-Wasek, R. Langlois, N. Sabarth, R. Konopitzky, F. Ramirez, K. Lehr, T. Mayr, et al. 2022. CD206+ tumor-associated macrophages cross-present tumor antigen and drive antitumor immunity. *JCI Insight*. 7:e155022. https://doi.org/10.1172/jci.insight.155022

Mujal, A.M., A.J. Combes, A.A. Rao, M. Binnewies, B. Samad, J. Tsui, A. Boissonnas, J.L. Pollack, R.J. Arguello, M.V. Meng, et al. 2022. Holistic characterization of tumor monocyte-to-macrophage differentiation integrates distinct immune phenotypes in kidney cancer. *Cancer Immunol. Res.* 10:403–419. https://doi.org/10.1158/2326-6066.CIR-21-0588

Naik, S., N. Bouladoux, J.L. Linehan, S.J. Han, O.J. Harrison, C. Wilhelm, S. Conlan, S. Himmelfarb, A.L. Byrd, C. Deming, et al. 2015. Commensal-dendritic-cell interaction specifies a unique protective skin immune signature. *Nature*. 520:104–108. https://doi.org/10.1038/nature14052

Nixon, B.G., F. Kuo, L. Ji, M. Liu, K. Capistrano, M. Do, R.A. Franklin, X. Wu, E.R. Kansler, R.M. Srivastava, et al. 2022. Tumor-associated macrophages expressing the transcription factor IRF8 promote T cell exhaustion in cancer. *Immunity*. 55:2044–2058.e5. https://doi.org/10.1016/j.immuni.2022.10.002

O'Brien, S.A., J. Orf, K.M. Skrzypczynska, H. Tan, J. Kim, J. DeVoss, B. Belmontes, and J.G. Egen. 2021. Activity of tumor-associated macrophage depletion by CSF1R blockade is highly dependent on the tumor model and timing of treatment. *Cancer Immunol. Immunother.* 70:2401–2410. https://doi.org/10.1007/s00262-021-02861-3

Park, M.D., I. Reyes-Torres, J. LeBerichel, P. Hamon, N.M. LaMarche, S. Hegde, M. Belabed, L. Troncoso, J.A. Grout, A. Magen, et al. 2023. TREM2 macrophages drive NK cell paucity and dysfunction in lung cancer. *Nat. Immunol.* 24:792–801. https://doi.org/10.1038/s41590-023-01475-4

Peranzoni, E., J. Lemoine, L. Vimeux, V. Feuillet, S. Barrin, C. Kantari-Mimoun, N. Bercovici, M. Guérin, J. Biton, H. Ouakrim, et al. 2018. Macrophages impede CD8 T cells from reaching tumor cells and limit the efficacy of anti-PD-1 treatment. *Proc. Natl. Acad. Sci. USA*. 115:E4041–E4050. https://doi.org/10.1073/pnas.1720948115

Pittet, M.J., M. Di Pilato, C. Garris, and T.R. Mempel. 2023. Dendritic cells as shepherds of T cell immunity in cancer. *Immunity*. 56:2218–2230. https://doi.org/10.1016/j.immuni.2023.08.014

Pittet, M.J., O. Michielin, and D. Migliorini. 2022. Clinical relevance of tumour-associated macrophages. *Nat. Rev. Clin. Oncol.* 19:402–421. https://doi.org/10.1038/s41571-022-00620-6

Qu, Y., J. Wen, G. Thomas, W. Yang, W. Prior, W. He, P. Sundar, X. Wang, S. Potluri, and S. Salek-Ardakani. 2020. Baseline frequency of inflammatory Cxcl9-expressing tumor-associated macrophages predicts response to avelumab treatment. *Cell Rep.* 32:107873. https://doi.org/10.1016/j.celrep.2020.107873

Ray, A., M. Bassette, K.H. Hu, L.F. Pass, B. Samad, A. Combes, V. Johri, B. Davidson, G. Hernandez, I. Zaleta-Linares, and M.F. Krummel. 2023. Multimodal identification of rare potent effector CD8 T cells in solid

tumors. *bioRxiv*. https://doi.org/10.1101/2023.09.26.559470 (Preprint posted September 28, 2023).

Ries, C.H., M.A. Cannarile, S. Hoves, J. Benz, K. Wartha, V. Runza, F. Rey-Giraud, L.P. Pradel, F. Feuerhake, I. Klaman, et al. 2014. Targeting tumor-associated macrophages with anti-CSF-1R antibody reveals a strategy for cancer therapy. *Cancer Cell*. 25:846–859. https://doi.org/10.1016/j.ccr.2014.05.016

Ruffell, B., D. Chang-Strachan, V. Chan, A. Rosenbusch, C.M. Ho, N. Pryer, D. Daniel, E.S. Hwang, H.S. Rugo, and L.M. Coussens. 2014. Macrophage IL-10 blocks CD8+ T cell-dependent responses to chemotherapy by suppressing IL-12 expression in intratumoral dendritic cells. *Cancer Cell*. 26:623–637. https://doi.org/10.1016/j.ccell.2014.09.006

Ruhland, M.K., E.W. Roberts, E. Cai, A.M. Mujal, K. Marchuk, C. Beppler, D. Nam, N.K. Serwas, M. Binnewies, and M.F. Krummel. 2020. Visualizing synaptic transfer of tumor antigens among dendritic cells. *Cancer Cell*. 37:786–799.e5. https://doi.org/10.1016/j.ccell.2020.05.002

Salmon, H., J. Idoyaga, A. Rahman, M. Leboeuf, R. Remark, S. Jordan, M. Casanova-Acebes, M. Khudoynazarova, J. Agudo, N. Tung, et al. 2016. Expansion and activation of CD103(+) dendritic cell progenitors at the tumor site enhances tumor responses to therapeutic PD-L1 and BRAF inhibition. *Immunity*. 44:924–938. https://doi.org/10.1016/j.immuni.2016.03.012

Schenkel, J.M., R.H. Herbst, D. Canner, A. Li, M. Hillman, S.L. Shanahan, G. Gibbons, O.C. Smith, J.Y. Kim, P. Westcott, et al. 2021. Conventional type I dendritic cells maintain a reservoir of proliferative tumor-antigen specific TCF-1^{+} CD8^{+} T cells in tumor-draining lymph nodes. *Immunity*. 54:2338–2353.e6. https://doi.org/10.1016/j.immuni.2021.08.026

Swierczak, A., A.D. Cook, J.C. Lenzo, C.M. Restall, J.P. Doherty, R.L. Anderson, and J.A. Hamilton. 2014. The promotion of breast cancer metastasis caused by inhibition of CSF-1R/CSF-1 signaling is blocked by targeting the G-CSF receptor. *Cancer Immunol. Res.* 2:765–776. https://doi.org/10.1158/2326-6066.CIR-13-0190

Szolnoky, G., Z. Bata-Csörgö, A.S. Kenderessy, M. Kiss, A. Pivarcsi, Z. Novák, K. Nagy Newman, G. Michel, T. Ruzicka, L. Maródi, et al. 2001. A mannose-binding receptor is expressed on human keratinocytes and mediates killing of Candida albicans. *J. Invest. Dermatol.* 117:205–213. https://doi.org/10.1046/j.1523-1747.2001.14071.x

Wei, J., Z. Chen, M. Hu, Z. He, D. Jiang, J. Long, and H. Du. 2021. Characterizing intercellular communication of pan-cancer reveals SPP1+ tumor-associated macrophage expanded in hypoxia and promoting cancer malignancy through single-cell RNA-seq data. *Front. Cell Dev. Biol.* 9:749210. https://doi.org/10.3389/fcell.2021.749210

White, J.R., R.A. Harris, S.R. Lee, M.H. Craigon, K. Binley, T. Price, G.L. Beard, C.R. Mundy, and S. Naylor. 2004. Genetic amplification of the transcriptional response to hypoxia as a novel means of identifying regulators of angiogenesis. *Genomics*. 83:1–8. https://doi.org/10.1016/S0888-7543(03)00215-5

Yofe, I., T. Shami, N. Cohen, T. Landsberger, F. Sheban, L. Stoler-Barak, A. Yalin, T.S. Phan, B. Li, L. Monteran, et al. 2023. Spatial and temporal mapping of breast cancer lung metastases identify TREM2 macrophages as regulators of the metastatic boundary. *Cancer Discov.* 13:2610–2631. https://doi.org/10.1158/2159-8290.CD-23-0299

Zheng, L., S. Qin, W. Si, A. Wang, B. Xing, R. Gao, X. Ren, L. Wang, X. Wu, J. Zhang, et al. 2021. Pan-cancer single-cell landscape of tumor-infiltrating T cells. *Science*. 374:abe6474. https://doi.org/10.1126/science.abe6474

JEM

Supplemental material

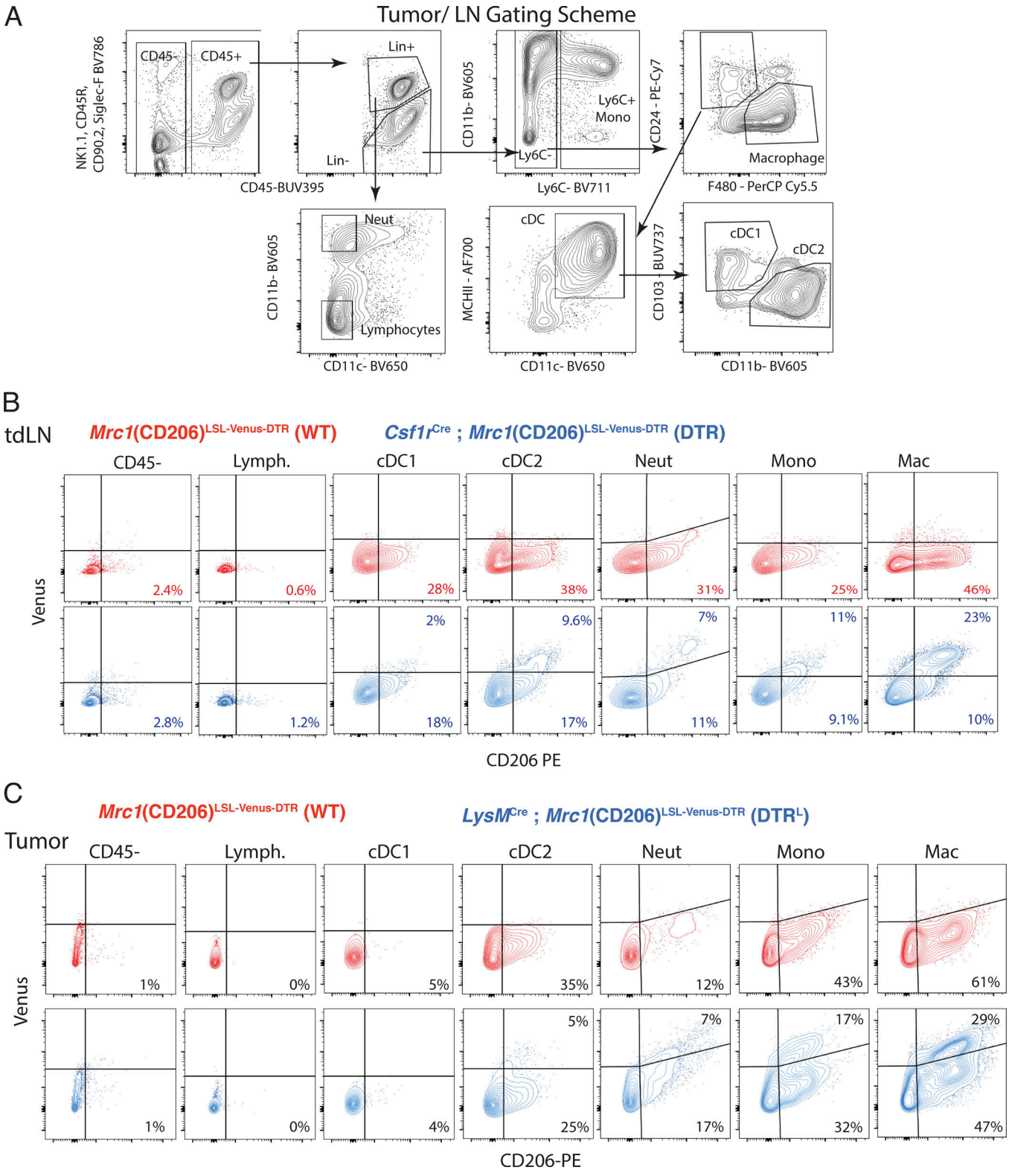

Figure S1. **Conditional CD206 reporter expression in various cell populations with distinct Cre drivers. (A–C)** Representative flow cytometry gating scheme to identify myeloid cells and lymphocytes from (A) tumor and tdLN; Flow cytometry plots showing reporter (Venus) and CD206 expression in different immune cell subsets in B d18 B78chOVA tdLN in (red; *Mrc1*(CD206)$^{LSL\text{-}Venus\text{-}DTR}$) and DTR (blue; *Csf1r*^{Cre}; *Mrc1*$^{LSL\text{-}Venus\text{-}DTR}$) mice and (C) B78chOVA tumor in WT (red: *Mrc1*$^{LSL\text{-}Venus\text{-}DTR}$) and DTR^{L} (blue: Lyz2(LysM)^{Cre}; *Mrc1*$^{LSL\text{-}Venus\text{-}DTR}$) mice. Data are representative of at least two independent experiments.

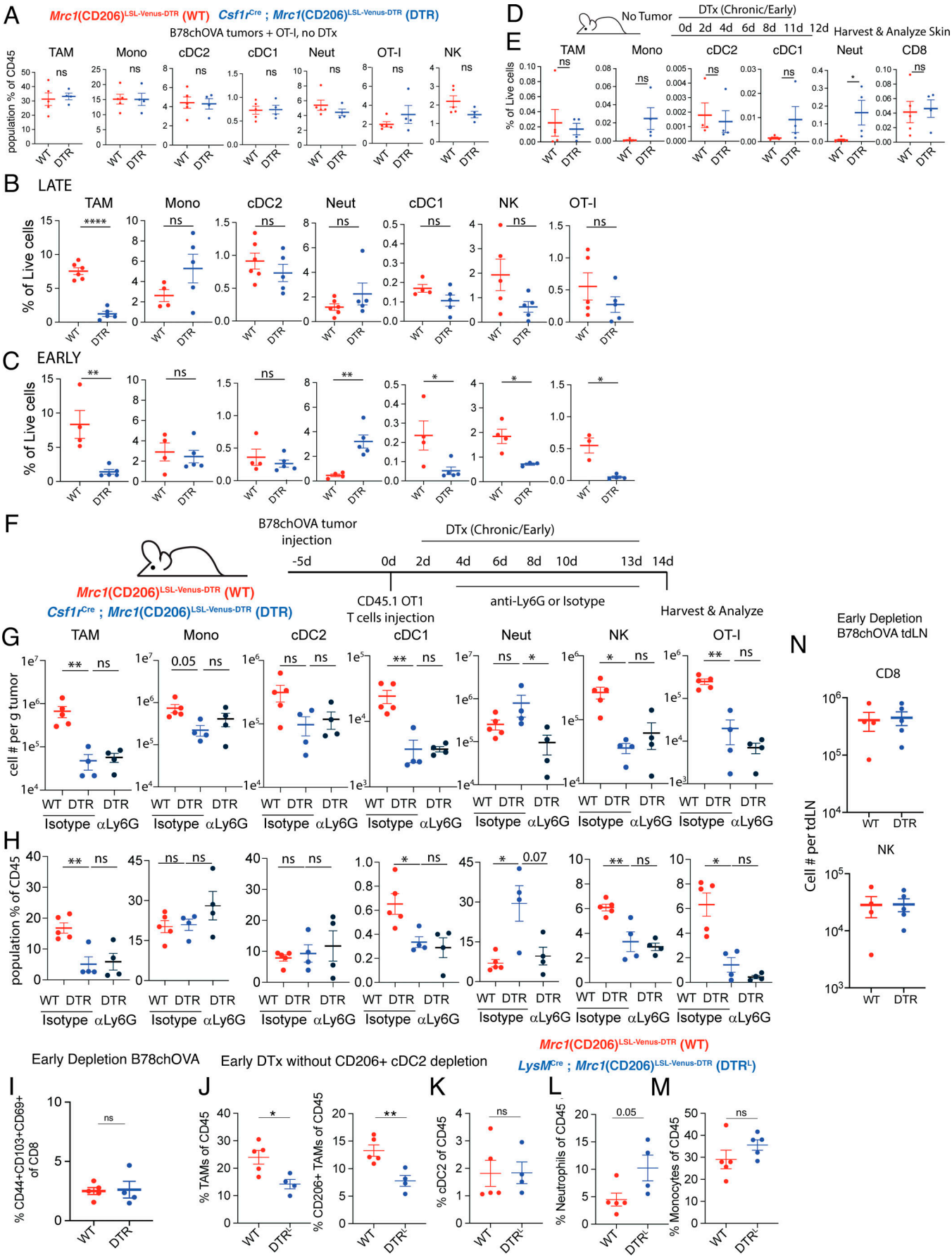

Figure S2. **Relative abundance of immune cells in control and reporter-expressing mice with DTx administration in different contexts. (A)** Relative abundance of different immune populations as a percentage of CD45$^+$ cells in *Mrc1*$^{LSL\text{-}Venus\text{-}DTR}$ (WT; red) and *Csf1r*^{Cre}; CD206$^{LSL\text{-}Venus\text{-}DTR}$ (DTR; blue) mice with B78chOVA tumor injection (day −5), OT-I adoptive transfer (day 0) and harvest (day 14) without DTx administration. **(B and C)** Relative abundance of different immune populations as a percentage of live cells with (B) late and (C) early depletion regimens by DTx treatment in B78chOVA tumors. **(D)** Schematic representation of the experimental setup for analysis of skin in *Mrc1*$^{LSL\text{-}Venus\text{-}DTR}$ (WT; red) and *Csf1r*^{Cre}; *Mrc1*$^{LSL\text{-}Venus\text{-}DTR}$ (DTR; blue) mice with DTx administration. **(E)** Relative abundance of different immune populations in the skin as a percentage of live cells. **(F)** Schematic representation of the experimental setup for B78chOVA tumor injection, OT-I T cell adoptive transfer, and early DTx administration with either isotype control or anti-Ly6G antibody treatment and analysis. **(G and H)** Abundance of different immune populations as (G) cells per g of tumor and (H) percentage of CD45$^+$ cells in WT and DTR mice in the above experiment. **(I)** Abundance of CD44$^+$CD103$^+$CD69$^+$ tissue-resident memory-like cells in B78chOVA tumors at day 18 in the early depletion setting. **(J–M)** In early DTx administration setting in WT (red; *Mrc1*$^{LSL\text{-}Venus\text{-}DTR}$) and DTR^L (blue; Lyz2(LysM)^{Cre}; *Mrc1*$^{LSL\text{-}Venus\text{-}DTR}$) mice, relative abundance of (J) TAMs and CD206$^+$ TAMs, (K) cDC2, (L) neutrophils, and (M) monocytes. **(N)** Number of CD8 T cells and NK cells per B78chOVA tdLN from WT and DTR mice at endpoint of early DTx treatment. Bar graphs show mean ± SEM; data are representative of at least two independent experiments, each with at least three biological replicates per group. ****P < 0.0001, **P < 0.01, *P < 0.05, ns = no significance by Student's *t* tests or Mann–Whitney test (A–C, E, and I–N), or Kruskal–Wallis test with post-hoc test correcting for false discovery (G and H).

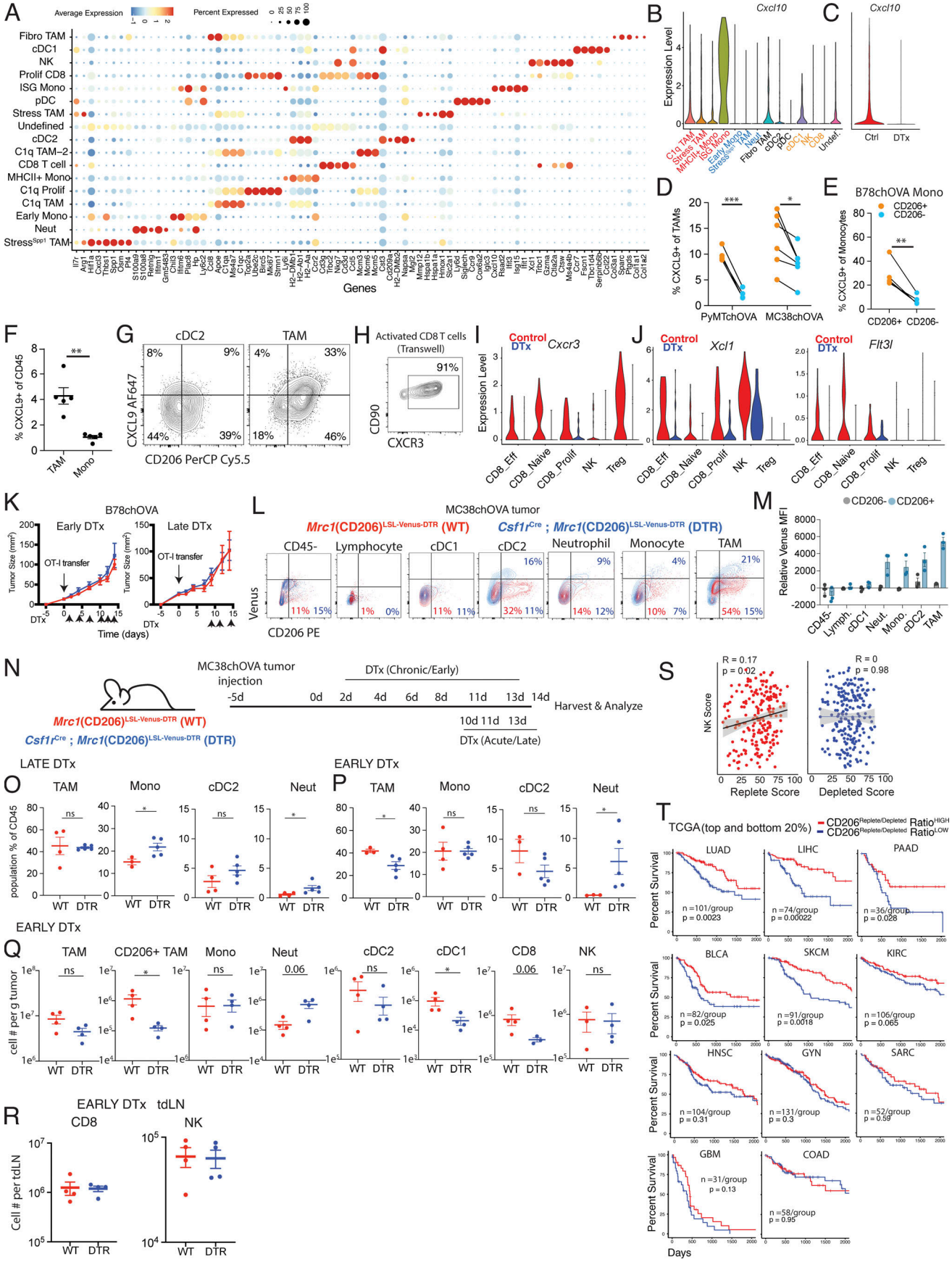

Figure S3. **Changes in chemokine expression and immune cell abundance in CD206-depleted tumors, and associated survival data in humans.** **(A)** Dotplot representing top five DEGs and select other genes in each immune cell cluster identified from a harmonized dataset of spatially barcoded Control and DTx treated B78chOVA tumors on day 12 after adoptive transfer of CD2dsRed; OT-I cells. **(B and C)** *Cxcl10* expression (B) aggregated across treatment conditions by cluster and (C) aggregated across clusters by treatment. **(D)** CXCL9 expression in PyMTchOVA and MC38chOVA (both without OT-I adoptive transfer) TAMs split by their CD206 expression. **(E and F)** (E) CXCL9 expression in B78chOVA intratumoral monocytes split by CD206 expression and (F) relative abundance of $CXCL9^+$ TAMs and monocytes in the same tumors. **(G)** Flow cytometry plot showing CD206 and CXCL9 expression in cDC2s and TAMs in B78chOVA tumors. **(H)** Percent of $CXCR3^+$ among in vitro activated CD8 T cells prior to transmigration in the presence of $CD206^-$ and $CD206^+$ TAMs. **(I and J)** Violin plot representing (I) *Cxcr3* and (J) *Xcl1* and *Flt3l* expression in the lymphoid compartment in Control and DTx treated conditions. **(K)** Tumor growth curves of B78chOVA tumors with OT-I adoption and early and late DTx administration. **(L and M)** (L) Overlaid flow cytometry plots showing reporter (Venus) and CD206 expression in different immune cells in MC38chOVA tumors in WT (red; $Mrc1^{LSL\text{-}Venus\text{-}DTR}$) and DTR (blue; $Csf1r^{Cre}$; $Mrc1^{LSL\text{-}Venus\text{-}DTR}$) mice and (M) quantification of relative reporter expression (DTR – WT) in the different subsets, split by CD206 expression. **(N)** Schematic representation of the experimental setup for early and late $CD206^+$ TAM depletion in MC38chOVA tumors using $Mrc1^{LSL\text{-}Venus\text{-}DTR}$ (WT) and $Csf1r^{Cre}$; $Mrc1^{LSL\text{-}Venus\text{-}DTR}$ (DTR) mice. **(O and P)** Relative abundance of different immune populations as a percentage of $CD45^+$ cells with (O) late and (P) early depletion regimens. **(Q)** Abundance of different immune populations as total number of cells per g of MC38chOVA tumor in WT and DTR mice in the early DTx administration regimen. **(R)** Number of CD8 T cells and NK cells per tdLN of WT and DTR mice with MC38chOVA tumors and treated with the early DTx regimen. **(S)** Scatter plots of the $CD206^{Replete}$ and $CD206^{Depleted}$ Mono/Mac score per patient with the NK cell score (Pearson R and P value for the null hypothesis that there is not a correlation are noted). **(T)** Kaplan–Meier survival curves of patients grouped by the value of the $CD206^{Replete}$: $CD206^{Depleted}$ signature ratio (top and bottom 20%) from TCGA split by indications, number of patients per group and P values for the log-rank test are noted for each curve in T. Bar graphs show mean ± SEM; data are representative of at least two independent experiments, each with at least three biological replicates, except the spatial transcriptomics data (A–C, I, and J), from one control and one DTx-treated tumor. ***P < 0.0001, **P < 0.01, *P < 0.05, ns = no significance by paired ratio *t* tests (D and E) or unpaired *t* tests or Mann–Whitney test in F and O–Q. *n* = 203 patients in S.